IEEE Access
Multidisciplinary | Rapid Review | Open Access Journal

Received 3 August 2024, accepted 20 August 2024, date of publication 26 August 2024, date of current version 4 September 2024.

Digital Object Identifier 10.1109/ACCESS.2024.3449913

RESEARCH ARTICLE

Modeling and Vibration Suppression of Rotating Machines Using the Sparse Identification of Nonlinear Dynamics and Terminal Sliding Mode Control

SINA PIRAMOON[1], (Member, IEEE), MOHAMMAD A. AYOUBI[2], (Senior Member, IEEE), AND SAEID BASHASH[3]

[1]Laboratory Products Division, Thermo Fisher Scientific, Santa Clara, CA 95054, USA
[2]Department of Mechanical and Aerospace Engineering, Santa Clara University, Santa Clara, CA 95053, USA
[3]Department of Mechanical Engineering, San José State University, San Jose, CA 95192, USA

Corresponding author: Mohammad A. Ayoubi (maayoubi@scu.edu)

This work was supported by Thermo Fisher Scientific Company Laboratory Equipment Division (LED), Santa Clara, CA, USA.

ABSTRACT This paper presents a novel physics-based data-driven approach for reconstructing the nonlinear governing equations and suppressing vibrations in vertical-shaft rotary machines during transient motion. We first identify the key nonlinear terms using a physics-based methodology. Subsequently, a data-driven approach, known as the Sparse Identification of Nonlinear Dynamical Systems (SINDy), is employed to reconstruct the nonlinear governing equations of a typical rotary machine. After validating the model, a robust nonlinear controller is designed using the terminal sliding mode control (TSMC) technique to reduce lateral vibrations in the machine's shaft. Extensive experimental tests on a laboratory-scale rotary system confirm the stability and robustness of the proposed approach. The results also demonstrate that the proposed method significantly reduces lateral vibrations in rotary machines.

INDEX TERMS Active vibration control, physics-based modeling, rotary machines, sparse identification of nonlinear dynamics (SINDy), terminal sliding mode control (TSMC).

I. INTRODUCTION

Excessive vibrations in the transient response of rotary systems can detrimentally impact performance, resulting in heightened wear and tear and even structural damage. While conventional control strategies have historically been utilized to mitigate these vibrations, recent advancements in data-driven techniques have amplified their importance.

The integration of data-driven models based on physics into traditional scientific computing and engineering design has garnered significant attention, primarily due to the availability of high-capacity datasets and advancements in numerical computation. This hybrid approach, known as physics-based data-driven modeling, harmonizes universal physical laws with data-based models derived from experimental data to enhance accuracy, robustness, and optimization across various domains [1]. These models merge the strengths of conventional physical models with the flexibility and adaptability inherent in data-driven methodologies. By utilizing empirical data to refine and enhance physical models, simulations and predictions can more closely align with real-world observations. This process provides a more precise representation of complex phenomena and facilitates improved scientific computing and engineering design. Furthermore, physics-based data-driven models have the potential to uncover valuable insights from data that may elude traditional modeling techniques alone, making them a promising avenue for advancing both scientific and control engineering.

Recent developments in data-driven control engineering have underscored the utilization of machine learning algorithms, such as deep learning and reinforcement learning, for

The associate editor coordinating the review of this manuscript and approving it for publication was Mouquan Shen.

control system design and optimization. Additionally, there is a growing focus on applying physics-based machine learning techniques in scientific computing, exploring how machine learning algorithms can be combined with physical laws and principles to enhance computational simulations and modeling [2]. A nonlinear dynamic optimization framework for learning governing equations from noise-contaminated state measurements over time highlights the potential for improved accuracy and efficiency in scientific computations [3]. Moreover, recent advances in data-driven modeling and control for complex systems delve into the use of techniques such as system identification and model predictive control across various application domains. Kaiser et al. underscore the potential of these approaches in enhancing system performance and adaptability [4].

Mathematical modeling plays a vital role in understanding the complexity of industrial systems, ensuring their control, and providing reliable representations. It enables the development of fault monitoring systems and robust control strategies, particularly for mitigating vibrations in rotating systems [5], [6]. With the advancement of data-driven science, there is a need to integrate these methodologies with physics-based methods, especially where modeling based on physical laws may have limitations. Accurate mathematical models are crucial for the active vibration control of rotary systems.

Finite Element Analysis (FEA) serves as a foundational approach in this field, enabling simulations of real-world phenomena encountered in rotating machinery. It allows for the analysis of a system's dynamic behavior and the identification of potential sources of vibration [7]. FEA-based models empower researchers to predict critical speeds, mode shapes, and various rotor vibration behaviors, thereby facilitating the identification of problematic modes [8]. FEA is widely adopted for the precise characterization of dynamic behavior in complex rotor systems [9]. It enables stress and modal analysis while accounting for rotational inertia, gyroscopic effects, and axial forces [10].

The nonlinear effects of bearing clearance and the investigation of vibratory behaviors in a vertical disk rotor supported by ball bearings are discussed in the context of general linear and nonlinear rotor modeling and rotor balancing [11]. Experimental validation confirms theoretical predictions and numerical simulations through methods such as modal analysis, vibration testing, and dynamic rotor balancing [12]. In a separate study, researchers conducted response analysis and examined transient vibrations of rotor systems under random and uncertain-but-bounded uncertainties, focusing on uncertainty quantification and transient response analysis [13]. Another study delved into the nonlinear dynamics of a rotor-ball bearing system with Alford force, emphasizing dynamic modeling and analysis of rotor systems supported by ball bearings [14].

Furthermore, a rotating machinery library for diagnosis was developed, incorporating models based on well-established rotor dynamics theory. This library provides specifications for various components of a rotary system, including motors, couplings, shafts, rotors, and bearings [15]. Theoretical analyses have extensively focused on assessing the impact of nonlinearity on vibration characteristics within controlled rotor systems. Numerical methods have been employed to meticulously scrutinize dynamic behavior and discuss the impact of absorber parameters [16].

In parallel, extensive investigations into the transient response of a speed-varying rotor subjected to sudden unbalance have been conducted. This approach included deriving time-dependent functions to model the loading process accompanying sudden unbalance and analyzing transient response characteristics across a spectrum of unbalanced parameters [16]. Additionally, researchers have developed theoretical models for nonlinear vibrations in flexible rotor-bearing systems, incorporating diverse dynamic elements and factors [17]. The database method in rotordynamic design has garnered significant attention, enabling precise predictions of bearing performance through nonlinear transient analysis [18].

Analytical studies have extensively explored the transient response of disk rotors, a pivotal aspect of rotor dynamics with notable contributions dating back to the pioneering work of Kirk and Gunter in 1972 [19]. Their research focused on analyzing dynamic unbalanced response and transient motion in single-mass disk rotors mounted on damped, flexible supports with elastic bearings. Their approach involved assuming synchronous precession and conducting a thorough steady-state analysis of both the shaft and the bearing housing motion. They further enhanced their study through numerical integration of motion equations, employing a modified 4th-order Runge–Kutta procedure [19]. In a study by [20], the focus was on investigating the transient response of a cracked rotor system. They developed a dynamic model based on a simple hinge crack model and conducted a detailed examination of the influence of factors such as unbalance and variations in stiffness on the transient response.

In a study by Ishida et al. [21], focusing on vibration suppression in nonlinear rotor disks and elastic shaft systems using dynamic dampers, researchers addressed resonance issues caused by machinery imbalance near critical speeds. The rotor system under investigation featured a single-row deep groove ball bearing, introducing nonlinear spring characteristics due to bearing clearance. To mitigate this, the study employed the Newton-Raphson method to optimize dynamic damper parameters for the nonlinear rotor, enabling passive vibration control. Researchers explored periodic motions and bifurcation trees in a buckled nonlinear disk rotor system [22]. Through numerical simulations, they examined the dynamic behavior and stability of the system. Additionally, research dedicated to nonlinear vibration control within a horizontally supported disk-rotor system was conducted [23]. The methodology included employing second-order approximate solutions and conducting bifurcation analyses to gain valuable insights into the effects of controller parameters.

Furthermore, effective analysis of transient responses in rotor systems can be achieved through the application of interval approaches and uncertainty analysis, as demonstrated by researchers [24]. Their strategy involved utilizing the nonintrusive Chebyshev interval method to analyze the transient response of rotor systems in the presence of uncertainty. They introduced a hybrid analysis procedure designed to mitigate calculation errors. Researchers [25] directed their focus toward the nonlinear dynamic behavior and stability of rotor/seal systems equipped with dynamic vibration absorbers.

Brunton et al. generalize the sparse identification of nonlinear dynamics (SINDy) algorithm to include external inputs and feedback control [26], [27]. They also demonstrate its application with model predictive control (MPC) using an infectious disease control example [28]. The research on active vibration control methods has gained prominence, employing strategies and actuators to counteract unbalanced forces [29]. Adaptive control strategies have been introduced to enhance rotor balance control, especially under variable speed conditions [30], utilizing feedback control algorithms to continuously adjust balancing forces and minimize vibrations. Various methods, including Active Force Control (AFC), have been employed to implement active vibration control in rotary systems, aiming to actively apply forces to counteract unbalanced forces and reduce vibrations [31]. Additionally, passive vibration control devices like inverters and dynamic vibration absorbers (DVA) have been integrated into rotary systems to enhance suspension performance [32].

The proposed SINDy method of system identification differs from existing techniques in the literature. Traditional methods such as the finite element method (FEM), Modal Analysis, and Eigensystem Realization Algorithm (ERA) each have strengths in certain domains [33]. FEM, a numerical technique for solving complex engineering problems by discretizing the system into elements, excels in detailed structural and dynamic behavior analysis but requires substantial computational resources and detailed modeling of geometry and materials. Modal Analysis extracts modal parameters from experimental or analytical models, suitable for linear systems with known modal properties but less effective for capturing nonlinear transient responses in rotary systems. ERA, a data-driven method for identifying linear state-space models from input-output data, reconstructs a model by estimating state and input matrices, effective for systems with small nonlinearities but challenging for more complex dynamics [34].

In contrast, the SINDy method provides a data-driven approach tailored for identifying nonlinear system dynamics and capturing complex behaviors directly from measured data. Leveraging sparse regression and model sparsity, SINDy offers a framework for nonlinear system identification, demonstrating efficacy in rotary system transient motion analysis and control. Recent research, such as uncertainty analysis and experimental validation of oscillator equation identification using sparse regression by Ren et al. [35], compares the performance of Least Squares Post-LASSO (LSPL) with the original SINDy method (LSST). LSPL outperforms LSST in terms of sparsity, convergence, identified eigenfrequency, and coefficient of determination, highlighting its practical potential in this domain.

The research by Bertsimas et al. [36] focuses on learning sparse nonlinear dynamics through mixed-integer optimization. They propose an exact formulation of the SINDy problem using mixed-integer optimization (MIO-SINDy) to achieve provably optimal solutions within seconds. This approach demonstrates the effectiveness of MIO in producing sparse solutions with strong predictive power, surpassing other widely used sparse learning techniques like Lasso. Such advancements hold promise for accurately identifying and learning sparse nonlinear dynamics, applicable across various fields requiring complex dynamic system modeling.

Recent publications have explored a diverse range of control strategies for rotor vibration suppression, including energy harvesting and adaptive control algorithms [37]. Sliding Mode Control (SMC) has emerged as a robust methodology for vibration suppression in various engineering applications [37]. Its application has been investigated in different contexts; for example, [38] studied robust active vibration suppression in a flexible beam using a sliding mode-based controller. Their research highlighted SMC's resilience to parameter variations and insensitivity to unmodeled dynamics, effectively managing beam vibrations. Experimental results demonstrated that the sliding mode controller reduced beam vibration more rapidly compared to proportional plus derivative (PD) control and lead compensation. In another study, [39] proposed and validated a robust nominal model-based sliding mode control approach for vibration suppression in a flexible rectangular plate. They implemented and validated this approach using MATLAB® and Simulink®, illustrating its effectiveness in vibration suppression. In [40], an overview of sliding mode control technology for permanent magnet synchronous motor systems is provided. It addresses topics such as chattering suppression, high-order sliding mode control, and terminal sliding mode control.

In [41], a practical terminal sliding-mode control method is proposed to rapidly stabilize a second-order plant with high precision, validated in real-time on a linear-motor-based control system for servo systems.

In this research, we initially utilized linear Sliding Mode Control (SMC) but revised our approach to Terminal Sliding Mode Control (TSMC) for faster convergence and enhanced performance. TSMC maintains robust sliding mode stability even in the presence of nonlinearities and model uncertainties, which is crucial for ensuring consistent performance in rotary machines under transient response vibrations. Developed as a robust control strategy, TSMC is particularly effective for systems encountering uncertainties, disturbances, and nonlinearities.

The main contributions of this paper lie in the realms of 1) modeling and 2) vibration suppression for a typical vertical

shaft rotary machine during transient motion. To the best of the authors' knowledge, no physics-informed, data-driven technique has been reported in the literature for modeling the transient response of rotary machines. Therefore, our approach and the outcomes of this research represent a novel contribution to the field.

To describe the proposed approach, we begin with the Lagrangian formulation of the equations of motion to identify the existing nonlinear terms within the governing equations. We then utilize these terms to establish a comprehensive mathematical library for the SINDy algorithm. Following this, we provide a concise overview of the mathematical foundations of the SINDy algorithm, which we employ to model the transient response of a two-degree-of-freedom rotary disk system. This modeling process uses real measured data for SINDy system identification. The framework of our approach is shown in Figure 1. Subsequently, the model is validated under various conditions, including acceleration and deceleration transient modes, while also accounting for induced rotor unbalancing and noise within the measured signal. Following validation, a nonlinear controller based on the terminal sliding mode control (TSMC) technique [42], [43], [44] is proposed, utilizing the validated SINDy model. The stability and performance of the closed-loop system are then examined using a laboratory test rig. Finally, we conclude the paper with some remarks.

II. NOTATIONS

Table 1 provides descriptions of the notations used in this paper.

III. PHYSICS-BASED MODELING OF ROTARY MACHINES

In this section, we employ physical laws to derive the equations of motion for the rotor system. The objective is to identify the nonlinear terms in the governing equations, construct a mathematical library, and utilize it in the data-driven algorithm.

A. SYSTEM MODELING

The lateral motion of a vertical shaft rotor system can be modeled by a two-degrees-freedom mass-spring-damper system, as depicted in Figure 2. The schematic illustrates a rotating imbalanced disk rotor, experiencing lateral vibrations in the plane perpendicular to its axis of rotation—normal to the plane.

Two reference frames are used to describe the intricate motion of the rotor. The $\mathcal{N}$-frame is the inertial reference frame fixed in space, and the $\mathcal{A}$-frame is a rotor-fixed frame with its origin located at the center of geometry, point C. The generalized coordinates, $q(t) \in \mathbb{R}^3$, is defined as $q = [x, y, \beta]^T$, where $x(t), y(t) \in \mathbb{R}$ represents the position of the disk center C and is measured from a fixed point O in the $\mathcal{N}$-frame and $\beta(t) \in \mathbb{R}$ is the angular position of the disk. The angle of vector $OC \in \mathbb{R}^2$ with the X-axis is $\gamma \in \mathbb{R}$. Due to the mass imbalance, the disk center-of-mass (CM) denotes by G has an offset distance e with respect to the reference frame

TABLE 1. Notations used in this paper.

Notation	Description
$\mathbb{R}, \mathbb{R}^+$	Set of Real and Positive Real Numbers
$\mathbb{N}, \mathbb{N}^+$	Set of Integer and Positive Integer Numbers
$m \in \mathbb{R}^+$	Mass of the Rotor
$J \in \mathbb{R}^+$	Moment of Inertia of the Rotor with respect to the Center of Rotation
$\bar{J} \in \mathbb{R}^+$	Moment of Inertia of the Rotor with respect to COM
$\beta(t) \in \mathbb{R}$	Rotor Angle of Rotation
$\dot{\beta}(t) \in \mathbb{R}$	Rotor Angular Velocity
$e \in \mathbb{R}^+$	Rotor Mass Eccentricity
$\tau_z \in \mathbb{R}$	Total Torque Applied on the Rotor-Bearing System
C_c	Bearing Coulomb Friction Coefficient
C_v	Rotor Viscous Damping Coefficient
C_a	Rotor Drag Friction Coefficient
$\mathbf{F}_s \in \mathbb{R}^{2\times 1}$	Stiffness Force
C	Damping Coefficient
$n \in \mathbb{N}^+$	Number of Sensors
$\mathbf{X}_m \in \mathbb{R}^{(p+4)\times n}$	Matrix of Sensor Measurements
$\mathbf{\Theta}(\mathbf{X}, t, \dot{\beta}) \in \mathbb{R}^{p\times q}$	SINDy Library of Mathematical Functions
$\mathbf{\Xi} \in \mathbb{R}^{q\times n}$	Matrix of SINDy Sparse Coefficients
$\mathcal{R} \in \mathbb{R}^{p\times 1}$	Column Vector of Nonlinear SINDy Library Functions
$S_x,\ S_y \in \mathbb{R}$	TSMC Sliding Manifolds in the X and Y Axes
$p,\ q$	Sliding Manifold Design Parameters (Positive odd integers with $p > q$)
$\mathcal{C}_1,\ \mathcal{C}_2 \in \mathbb{R}^+$	Terminal Sliding Manifold Design Parameters
$\rho_1,\ \rho_2 \in \mathbb{R}^+$	Terminal Sliding Manifold Design Tuning Parameters
$V(X) \in \mathbb{R}^+$	Lyapunov Function
$U_x,\ U_y \in \mathbb{R}$	TSMC Lateral Control Signals in the X and Y Axes
$\Delta_x,\ \Delta_y$	Uncertainty with Known Upper Bound $\rho_1,\ \rho_2$
X_1	X-axis displacement, state x
X_2	X-axis velocity, state $\dot{x}$
X_3	Y-axis displacement, state y
X_4	Y-axis velocity, state $\dot{y}$
X_5	Angular displacement, state β
X_6	Angular velocity, state $\dot{\beta}$

$\mathcal{A}$. For simplicity, we assume vector CG is aligned with a_1 in the body frame $\mathcal{A}$. An AC electric motor applies torque $\tau_m \in \mathbb{R}$ to spin the rotor. A pair of perpendicular control forces $U_X \in \mathbb{R}$ and $U_Y \in \mathbb{R}$ are applied to the disk to regulate lateral plane vibration. For control of the lateral vibration, the control force $u(t) \in \mathbb{R}^2$ is defined as $u = [U_X,\ U_Y]^T$. Let's use the Lagrange method and derive the equations of motion as follows,

$$\frac{d}{dt}\left(\frac{\partial \mathcal{L}}{\partial \dot{q}_i}\right) - \frac{\partial \mathcal{L}}{\partial q_i} = Q_i, \quad (i = 1, 2, 3), \tag{1}$$

where $\mathcal{L}$ is the Lagrangian, $\mathcal{L} = T - V$, T represents the kinetic energy, and V represents the potential energy

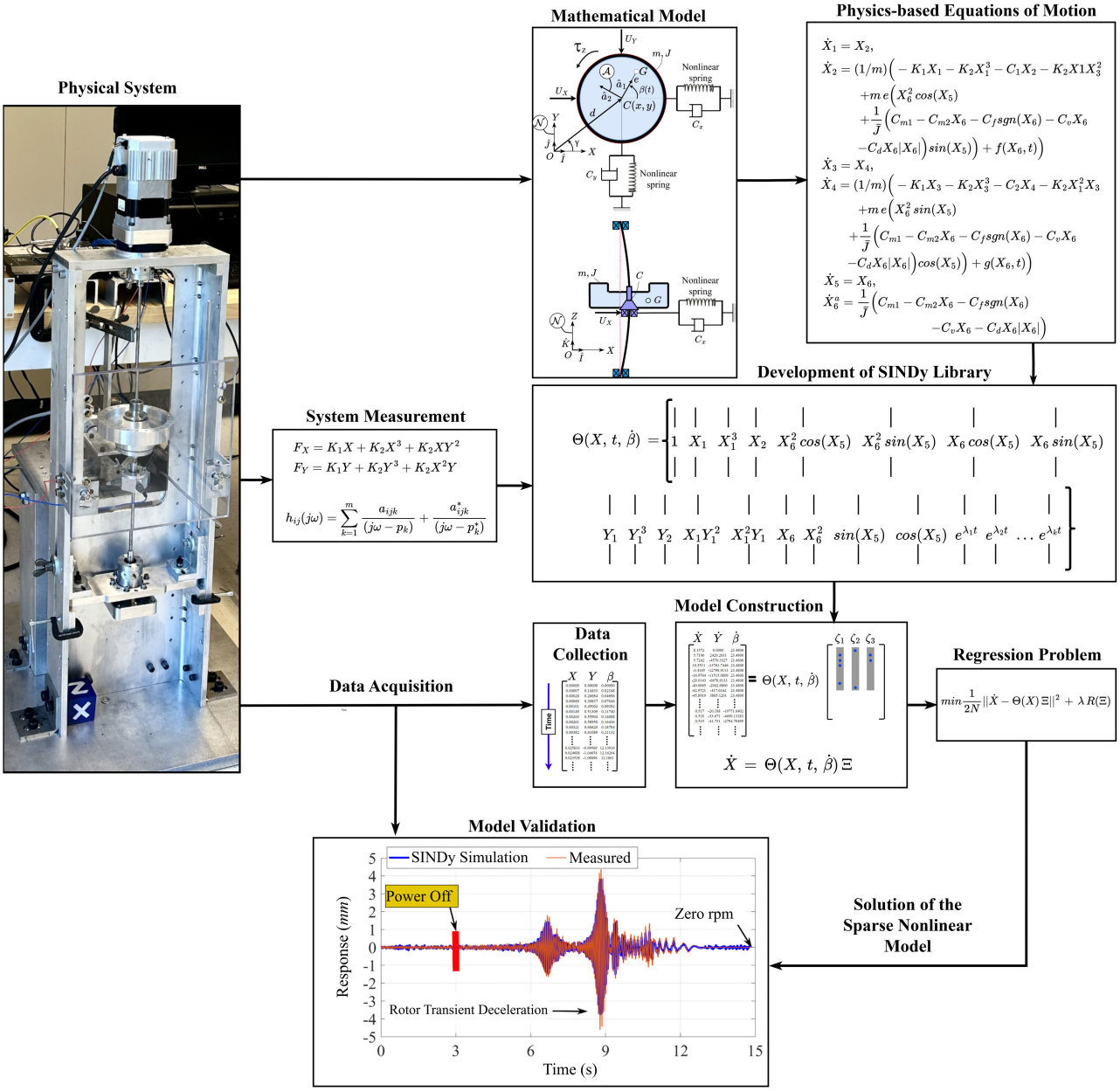

FIGURE 1. The framework for integrating physics-based and data-driven approaches.

of the system. Q_i represents the generalized forces, and q_i represents the generalized coordinates. For the Lagrangian $\mathcal{L}$, we compute both the translational and rotational kinetic energies of the rotor, given by $T = T_r + T_t$, where T_r is the rotational kinetic energy and T_t is the translation part of the total kinetic energy. The kinetic energy of the rotor can be found from

$$\begin{aligned} T &= \frac{1}{2} m \left({}^{\mathcal{N}}\vec{V}^{\,G} \cdot {}^{\mathcal{N}}\vec{V}^{\,G} \right) + \frac{1}{2} \bar{J}\, \dot{\beta}^2 \\ &= \frac{1}{2} m \Big[\dot{x}^2 + \dot{y}^2 + e^2\, \dot{\beta}^2 \\ &\quad + 2e\, \dot{\beta} (-\dot{x}\, \sin\beta + \dot{y}\, \cos\beta) \Big] + \frac{1}{2} \left(J - m\, e^2 \right) \dot{\beta}^2, \end{aligned} \tag{2}$$

where $m \in \mathbb{R}^+$ and $J \in \mathbb{R}^+$ are the mass and the moment of inertia of the rotor with respect to the center of geometry C. The moment of inertia of the rotor with respect to the center of mass G is denoted as $\bar{J}$. The relationship $J = \bar{J} + m\,e^2$ holds, where e is the distance between the center of geometry C and the center of mass G. The position and velocity vectors can be found from

$$\vec{R}^{\,OG} = \vec{d} + e\hat{a}_1 = x\hat{I} + y\hat{J} + e\hat{a}_1, \tag{3}$$

and the velocity of the center of mass is

$$\begin{aligned} {}^{\mathcal{N}}\vec{V}^{\,G} &= \frac{{}^{\mathcal{N}}d}{dt} \left({}^{\mathcal{N}}\vec{R}^{\,G} \right) = \left(\dot{x} - e\, \dot{\beta}\ \sin\beta \right) \hat{I} \\ &\quad + \left(\dot{y} + e\, \dot{\beta}\ \cos\beta \right)\ \hat{J}. \end{aligned} \tag{4}$$

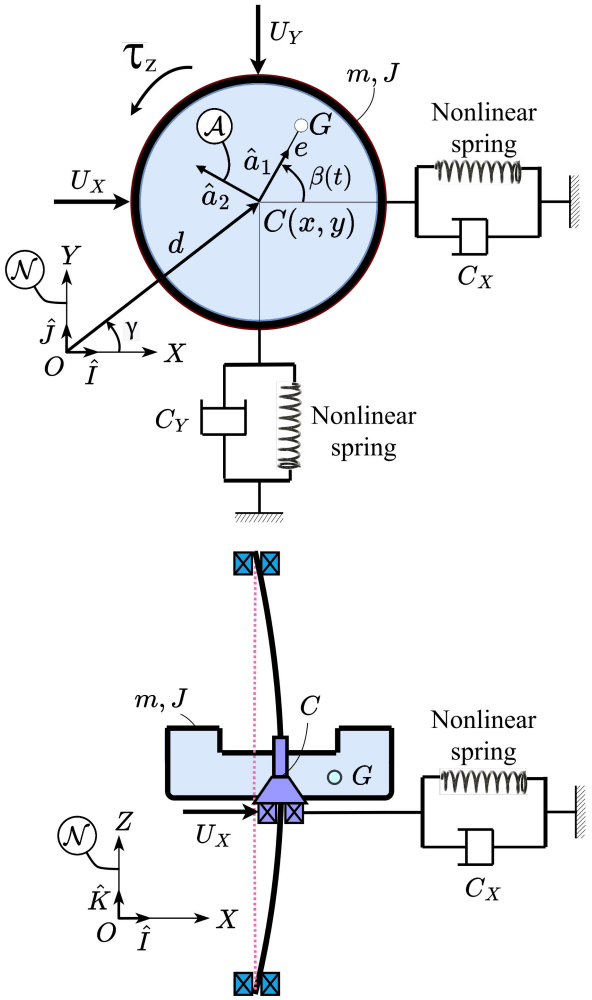

FIGURE 2. Illustration of the top and front view of a two-degrees-of-freedom model of a rotary disk. This model includes imbalance mass, lateral nonlinear stiffness and damping, and control forces along the *X*- and *Y*-axes.

The potential energy change due to gravity is zero.

By reference to (1), the equation of motion for the rotor of Figure 2 can be written as,

$$\Sigma : \begin{cases} \ddot{x} = e\ddot{\beta}\sin\beta + e\dot{\beta}^2\cos\beta - \dfrac{F_{sX}}{m} - \dfrac{C_X\dot{x}}{m} + \dfrac{U_X}{m}, \\ \ddot{y} = -e\ddot{\beta}\cos\beta + e\dot{\beta}^2\sin\beta - \dfrac{F_{sY}}{m} - \dfrac{C_Y\dot{y}}{m} + \dfrac{U_Y}{m}, \\ \bar{J}\ddot{\beta} = \tau_z, \end{cases} \tag{5}$$

where $F_{sX}, F_{sY} \in \mathbb{R}$ represent nonlinear stiffness forces and τ_z is given by

$$\tau_z = \tau_m - (\tau_c + \tau_v + \tau_a), \tag{6}$$

in which the Coulomb friction torque, τ_c, at the bearing is

$$\tau_c = C_c\,\mathrm{sign}(\dot{\beta}), \tag{7}$$

where C_c is the Coulomb friction coefficient. The viscous damping torque,τ_v, at bearings is assumed to be in the form of

$$\tau_v = C_v\,\dot{\beta}, \tag{8}$$

where C_v is the viscous damping coefficient and the aerodynamic damping torque, τ_a, a model which represents the drag of air resistance with the surface of the rotor is

$$\tau_a = C_a\,\dot{\beta}\,|\dot{\beta}|, \tag{9}$$

where C_a is the aerodynamic damping coefficient. The driving torque applied by the motor, $\tau_m \in \mathbb{R}$ is given by [47],

$$\tau_m = \frac{K_t}{R}V - \frac{K_tK_b}{R}\dot{\beta}, \tag{10}$$

where V is the voltage, R is the motor resistance, and K_t, $K_b \in \mathbb{R}$ are the torque and back EMF constants which are physical parameters associated with the motor. Because our motor is powered by a constant voltage source during acceleration, we can rewrite (10) as

$$\tau_m = C_{m1} - C_{m2}\,\dot{\beta}, \tag{11}$$

and during deceleration, $\tau_m = 0$.

By observation and measurement, we noticed that the stiffness behavior is nonlinear. A system measurement was conducted on the system shown in Figure 2, to identify the mathematical model of the forces F_{sX}, F_{sY}. In the following section, the nonlinear stiffness model is determined by experiment.

B. MEASURING SYSTEM'S LATERAL STIFFNESS

We measured the elastic deflection of the rotor by applying lateral force and measured the static displacement of the rotor as shown in Figure 3. To this end, we use a Wagner-FDX-50 digital force sensor (item 1 in Figure 3) to apply force to the flexible shaft rotor and used a Mitutoyo-2046S displacement indicator (item 2 in Figure 3) to measure the displacement in an arbitrary direction. The results of force versus displacement measurements are shown in Figure 4. It was observed that the relation between the force and displacement follows a cubic polynomial in an arbitrary direction, i.e.,

$$F_s = K_1 d + K_2 d^3. \tag{12}$$

For the equivalent stiffness in the X- and Y-axes, the relations $x = d\cos\gamma$ and $y = d\sin\gamma$ are employed. After some algebraic manipulation, we obtain,

$$\begin{aligned} F_{sX} &= F_s\cos\gamma = K_1 x + K_2\,x\left(x^2 + y^2\right), \\ F_{sY} &= F_s\sin\gamma = K_1 y + K_2\,y\left(x^2 + y^2\right). \end{aligned} \tag{13}$$

It is worth mentioning here that the experimental results confirm that the damping forces are linear.

IV. DATA-DRIVEN MODELING OF ROTARY MACHINE

This section provides a brief review of the SINDy algorithm. Then, by utilizing the equations of motion derived from the physics-based approach, we construct a mathematical library and reconstruct the governing equations.

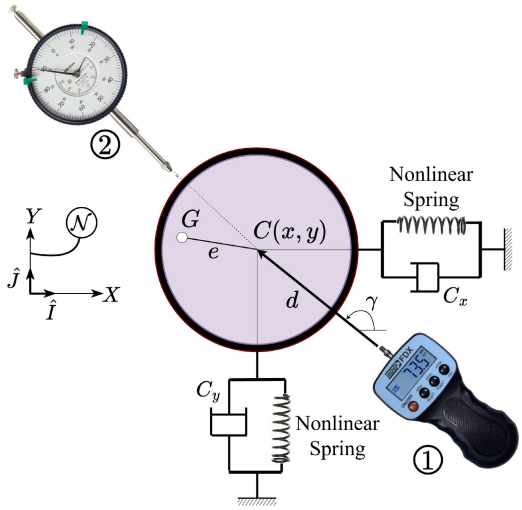

FIGURE 3. Experimental stiffness measurement using the Wagner-FDX-50 Digital Force Sensor ① for applied force measurement and the Mitutoyo-2046S Displacement Indicator ② for displacement measurement in the same direction.

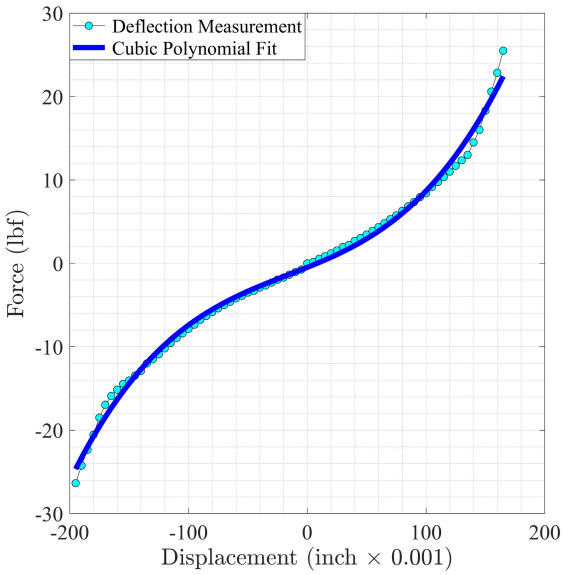

FIGURE 4. The force vs. deflection plot of the rotor drive shaft.

A. A BRIEF OVERVIEW OF THE SINDY ALGORITHM

Sparse Identification of Nonlinear Dynamics (SINDy) is a data-driven approach widely employed for discovering the dynamics of complex systems. The SINDy algorithm has demonstrated its versatility by successfully revealing underlying dynamics in various contexts, including fluid vortex shedding behind an obstacle [26] and other scientific studies [2]. Its adaptability extends beyond time-invariant systems, as it can effectively handle parameterized systems and those with time-varying dynamics or external forcing [2].

The SINDy algorithm employs a library of potential functions that may appear in the system's differential equations, encompassing constants, trigonometric functions, polynomials, and elementary functions. Through the application of sparse regression techniques, SINDy meticulously selects the most relevant terms from this library to construct a concise model capturing the observed data dynamics [26]. It employs techniques such as L_1 regularization and compressed sensing to promote sparsity and estimate the coefficients of the selected terms. This process facilitates the extraction of a simplified yet accurate mathematical model from high-dimensional and noisy data. This approach facilitates the discovery of governing equations through a data-driven method.

The typical workflow for applying SINDy involves several key steps: preprocessing the available data (including filtering, noise reduction, and feature extraction), constructing a library of candidate functions, employing sparse regression techniques to identify relevant terms and estimate their coefficients, validating the resulting model using root mean square error (RMSE) to compare measured and modeled data, and ultimately using the identified nonlinear state-space model for various purposes, such as analysis, prediction, control, or optimization. In the previous section, Lagrangian mechanics is employed to identify the general form of the governing equations and build a mathematical function library for the SINDy.

We sample $\mathbf{X}_m \in \mathbb{R}^{(p+4)\times n}$ measurements, where $n \in \mathbb{N}^+$ is the number of sensors or the number of states from which we aim to derive their dynamical equations, and $p \in \mathbb{N}^+$ represents equitime discrete measurement data. These measurements are then arranged in a matrix where each column represents a vector of measurements from a state or a sensor, as follows:

$$\mathbf{X}_m = \begin{bmatrix} x_1(t_1) & x_2(t_1) & x_3(t_1) & \dots & x_n(t_1) \\ x_1(t_2) & x_2(t_2) & x_3(t_2) & \dots & x_n(t_2) \\ x_1(t_3) & x_2(t_3) & x_3(t_3) & \dots & x_n(t_3) \\ \dots & \dots & \dots & \ddots & \dots \\ x_1(t_{p+4}) & x_2(t_{p+4}) & x_3(t_{p+4}) & \dots & x_n(t_{p+4}) \end{bmatrix}. \quad (14)$$

If h is considered as the time step between each measurement, fourth-order central difference numerical differentiation can be employed to compute the derivative in each column of the matrix $\mathbf{X}_m$. The fourth-order central difference formula is given by

$$\frac{dx_j}{dt} \approx \frac{-x_j(i+2) + 8x_j(i+1) - 8x_j(i-1) + x_j(i-2)}{12h}, \quad (15)$$

in which $(j = 3, \cdots, p-2)$ is used to denote the numerical derivatives of the matrix $\mathbf{X}_m$. Then, the matrix of derivatives is represented as follows:

$$\dot{\mathbf{X}}_m \approx \frac{d\mathbf{X}_m}{dt} \in \mathbb{R}^{p\times n}. \quad (16)$$

In real-time measurements, the time samples $\mathbf{X}_m$ may be contaminated with noise. Depending on the nature of the

noise, it might be necessary to filter both the data $\mathbf{X}_m$ and its derivative $\dot{\mathbf{X}}_m$. We used Gaussian filtering, which involves applying a Gaussian function to the measured signal to convolve it, effectively reducing high-frequency noise while preserving the overall shape and important features of the data [45].

Next, we build a library of candidate functions for the states $\mathbf{X}$ and time, highlighting the rotor angular velocity $\dot{\beta}$ as a crucial parameter for distinguishing a candidate function for a rotary system. The mathematical representation is presented as follows:

$$\boldsymbol{\Theta}(\mathbf{X}, t, \dot{\beta}) = \left[\mathcal{R}_1 \ \mathcal{R}_2 \ \mathcal{R}_3 \ \ldots \ \mathcal{R}_q\right], \tag{17}$$

where $\boldsymbol{\Theta}(\mathbf{X}, t, \dot{\beta}) \in \mathbb{R}^{p\times q}$ is a matrix of $p \times q$ candidate nonlinear functions with $q \in \mathbb{N}^+$ equal to the number of terms in the library, and $\mathcal{R}_1, \ldots, \mathcal{R}_q \in \mathbb{R}^{p\times 1}$ are column vectors of nonlinear candidate functions. The idea is to form a system of equations similar to the matrix system of linear equations $\mathbf{AX} = \mathbf{b}$, where $\mathbf{b}$ matrix are the $\dot{\mathbf{X}}$ terms and the $\mathbf{A}$ matrix is the $\boldsymbol{\Theta}(\mathbf{X}, t, \dot{\beta})$ library. The designed data-driven system is formed by the assembly of the matrices,

$$\dot{\mathbf{X}}_m = \boldsymbol{\Theta}(\mathbf{X}, t, \dot{\beta}) \ \boldsymbol{\Xi}. \tag{18}$$

Using the data matrix $\boldsymbol{\Theta}$, there are q solutions computed in the matrix $\boldsymbol{\Xi} = [\xi_1, \xi_2, \xi_3, \ldots, \xi_q]^T \in \mathbb{R}^{q\times n}$, where the superscript T denotes the transpose of a vector. To find a model, we apply the least absolute shrinkage and selection operator (LASSO), which solves the following convex l_1-regularized sparse regression objective function [48]:

$$\xi_k = \arg\min_{\xi_k'} \left(\|\dot{X}_{mk} - \Theta(X, t, \dot{\beta})\xi_k'\|_2 + \lambda\|\xi_k'\|_1\right). \tag{19}$$

Here, $\|\cdot\|_p$ denotes the p-norm of a matrix, $\dot{X}_{mk}$ is the k-th column of $\dot{X}$, and λ is a sparsity-promoting parameter. LASSO identifies a sparse coefficient matrix Ξ that selects the most important terms from the library of candidate functions, thereby discovering the underlying sparse dynamics of the system.

In SINDy, we assume that the underlying dynamics of the system can be approximated by a sparse linear combination of nonlinear basis functions, providing a mathematical tool to analyze highly nonlinear systems, such as the transient motion of rotary systems. A critical aspect of this technique lies in identifying the appropriate mathematical library or basis functions tailored to the specific problem at hand. Our approach addresses this challenge by employing the Lagrange equations of motion, grounded in physical laws. Additionally, the performance of SINDy relies on the quality and quantity of available data. Insufficient or noisy data can lead to poor model identification and inaccurate predictions. Furthermore, the effectiveness of SINDy can vary depending on system complexity, dimensionality, and the nature of the underlying dynamics. The reconstructed model from SINDy may not always generalize well to unseen data or different operating conditions. Overfitting to the training data and limited robustness to perturbations are common challenges that affect the model's generalizability. During our investigation, we noticed that incorporating natural frequencies within the SINDy model not only improves the discovered model's accuracy but also enhances the model's resilience to noise, leading to superior performance in experiments. The following describes the process of finding the natural frequencies of the rotor system.

B. MEASURING SYSTEM'S NATURAL FREQUENCIES

Measuring the natural frequencies of a system is achieved through the Frequency Response Function (FRF) technique. This method involves analyzing the system's response to an applied force at various frequencies to determine its natural frequencies and mode shapes. Natural frequencies are the frequencies at which a structure vibrates, while mode shapes describe the spatial distribution of vibrations within the structure. In this paper, we focus on measuring the rotor natural frequencies and formulating them within the SINDy library to determine the coefficients, which represent the weight of each term in the library. Modal hammer testing is commonly employed for identifying a system's natural frequencies. In experimental modal testing, sensors are utilized to measure the structural response to excitation, and the natural frequencies and mode shapes are derived from the collected data [46].

To achieve this, we set up a modal test as shown in Figure 5. The DAQ Spider-20 from Crystal Instruments was employed in conjunction with a Dytran accelerometer sensor (Model 3056D11T), featuring a sensitivity of 50 mV/g and a range of 100 $\times$ g acceleration. Additionally, a modal hammer (Model 5800B2T) was used, which has a sensitivity of 100 mV/lbf and a range of 50 lbf.

A practical guide provided by [46] outlines the computation point-to-point frequency response functions by analyzing the response at point i when subjected to an input at point j. This approach is conceptually similar to that of a single-degree-of-freedom system, with the key distinction being the summation of the effects of all modes. In the case of a planar disk rotor, the frequency response function is composed of a combination of single-degree-of-freedom systems, accounting for the contributions of all system modes. For the system's frequency response function for a specific input-output location ij, the following equation is employed [46]:

$$h_{ij}(j\omega) = \text{Lower residuals} + \sum_{k=1}^{m} \frac{a_{ijk}}{(j\omega - p_k)} + \frac{a_{ijk}^*}{(j\omega - p_k^*)} + \text{Upper residuals}, \tag{20}$$

where, $h_{ij}(j\omega) \in \{\mathbb{C} = a + i\,b \mid a, b \in \mathbb{R}, i^2 = -1\}$, the frequency variable $\omega\,(rad/s) \in \mathbb{R}$, the residuals $a_{ijk}, a_{ijk}^* \in \mathbb{C}$ and system poles $p_k, p_k^* \in \mathbb{C}$, where $(*)$ is the complex conjugate term. Figure 6 displays the band of interest, which

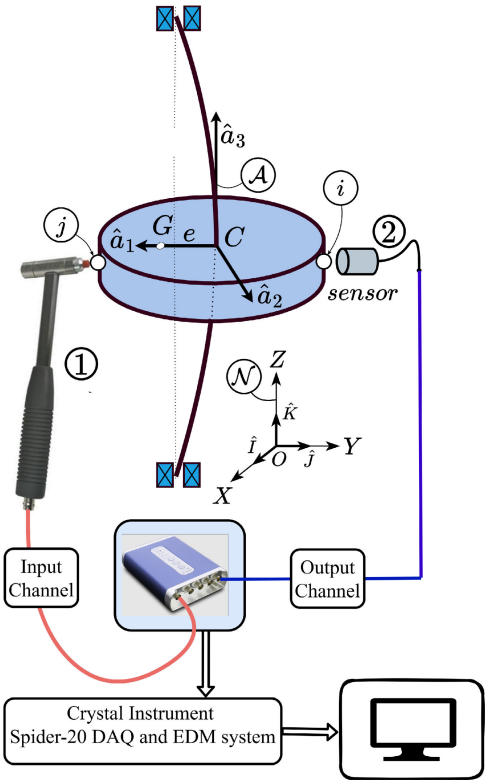

FIGURE 5. Experimental modal analysis of rotor system utilizing the modal hammer model 5800B2T with sensitivity of 100 *mV*/*lbf* and 50 *lbs* range ① for applied impact force in the *X*-axis. The Dytran 3056D11T accelerometer has a sensitivity of 50 *mV*/*g* with 100 × *g* range sensor ②.

is a selection of the first 35 modes of vibrations. The modal testing results in the solution of the frequency response function (20), identifying the natural frequencies of the system for the SINDy library. These modes and residuals are essential for refining the model and ensuring a more accurate representation of the system's behavior using the SINDy algorithm.

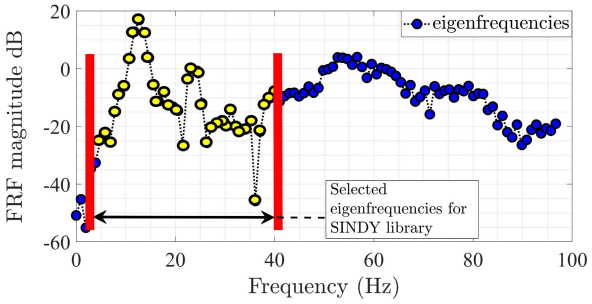

FIGURE 6. Frequency response function plot of the rotor system derived from the experimental modal testing.

C. RECONSTRUCTING THE ROTOR DIFFERENTIAL EQUATIONS

Considering (5) and utilizing the measurements from previous sections, the system of differential equations for the rotor system during acceleration, Σ_a, can be written as

$$\Sigma_a : \begin{cases} \dot{X}_1 = X_2, \\ \dot{X}_2 = (1/m)\Big\{ -K_1X_1 - K_2X_1^3 - \\ \quad C_1X_2 - K_2X_1X_3^2 + \\ \quad m\,e\Big[X_6^2\cos(X_5) + (1/\bar{J})\Big(C_{m_1} - C_{m_2}X_6 - \\ \quad C_c sgn(X_6) - C_vX_6 - C_aX_6|X_6|\Big)\sin(X_5)\Big] + \\ \quad f(X_6,t)\Big\}, \\ \dot{X}_3 = X_4, \\ \dot{X}_4 = (1/m)\Big\{ -K_1X_2 - K_2X_3^3 - \\ \quad C_2X_4 - K_2X_1^2X_3 + \\ \quad m\,e\Big[X_6^2\ \sin(X_5) - (1/\bar{J})\Big(C_{m_1} - C_{m_2}X_6 - \\ \quad C_c sgn(X_6) - C_vX_6 - C_aX_6|X_6|\Big)\cos(X_5)\Big] + \\ \quad g(X_6,t)\Big\}, \\ \dot{X}_5 = X_6, \\ \dot{X}_6 = (1/\bar{J})\Big[C_{m_1} - C_{m_2}X_6 - C_c sgn(X_6) - C_vX_6 - \\ \quad C_aX_6|X_6|\Big], \end{cases} \tag{21}$$

in which the state vector of the system is defined as

$$X \triangleq [x, \dot{x}, y, \dot{y}, \beta, \dot{\beta}]^T. \tag{22}$$

The functions $f(X_6,t)$ and $g(X_6,t)$ represent the terms in the form of $e^{\lambda_i t}, (i = 1, \cdots, 35)$, in the X and Y-axes, respectively. These terms did not explicitly appear in (5).

Similarly, we can show that the system model for rotor transient deceleration, Σ_d, can be written as:

$$\Sigma_d : \begin{cases} \dot{X}_1 = X_2, \\ \dot{X}_2 = (1/m)\Big\{ -K_1X_1 - K_2X_1^3 - C_1X_2 \\ \quad -K_2X_1X_3^2 + m\,e\Big[X_6^2\ \cos(X_5) + \\ \quad (1/\bar{J})\Big(-C_c sgn(X_6) - C_vX_6 - \\ \quad C_aX_6|X_6|\Big)\sin(X_5)\Big] + f(X_6,t)\Big\}, \\ \dot{X}_3 = X_4, \\ \dot{X}_4 = (1/m)\Big\{ -K_1X_3 - K_2X_3^3\ - C_2X_4 \\ \quad -K_2X_1^2X_3 + m\,e\Big[X_6^2\ \sin(X_5) \\ \quad -(1/\bar{J})\Big(-C_c sgn(X_6) - C_vX_6 - \\ \quad C_aX_6|X_6|\Big)\cos(X_5)\Big] + g(X_6,t)\Big\}, \\ \dot{X}_5 = X_6, \\ \dot{X}_6 = (1/\bar{J})\Big[-C_c sgn(X_6) - C_vX_6 - C_aX_6|X_6|\Big]. \end{cases} \tag{23}$$

By leveraging the nonlinear terms in (21) and (23), we construct a mathematical library for the SINDy algorithm. The implementation of Lagrangian mechanics serves as a framework for generating candidate functions for SINDy

library. Its implementation provides a set of nonlinear functions for performing sparse regression and model discovery from rotor transient response data. The SINDy dictionary for modeling lateral vibration in rotary systems is demonstrated in the following mathematical expressions:

$$\begin{aligned}\boldsymbol{\Theta}(\mathbf{X}, t, \dot{\beta}) = \Big[& 1 \quad X_1 \quad X_1^3 \quad X_2 \\ & X_6^2 \cos X_5 \quad X_6^2 \sin X_5 \\ & X_6 \cos X_5 \quad X_6 \sin X_5 \\ & Y1 \quad Y_1^3 \quad Y_2 \\ & X_1 Y_1^2 \quad X_1^2 Y_1 \\ & X_6 \quad X_6^2 \\ & \sin X_5 \quad \cos X_5 \\ & e^{\lambda_1 t} \quad e^{\lambda_2 t} \quad e^{\lambda_3 t} \ldots \quad e^{\lambda_k t} \Big] \in \mathbb{R}^{p \times q}. \end{aligned} \tag{24}$$

The SINDy process for rotary system modeling is shown in Figure 1. Next, the displacement of the disk center, denoted as (x, y), is measured with a sampling rate of 1 kHz during $10 - 15$ seconds, resulting in a total of $10,000$ to $15,000$ samples. During the test, the lateral control forces are set to zero, i.e., $U_X = U_Y = 0$. Using this measured data, the matrix X_m is formed as described in Subsection IV-A, and the procedure outlined there is applied to reconstruct the system's governing equations. The outcome is a parsimonious model generated through regression. In the following section, the reconstructed model is validated using experimental data for various cases.

V. MODEL VALIDATION

We utilize distinct sets of experimental data to evaluate the accuracy and robustness of the derived SINDy model in both startup (acceleration) and shutdown (deceleration) scenarios, considering the presence of measurement noise and imbalance masses. Figures 7 and 8 show the comparison between the model prediction and experimental data during startup and shutdown, respectively.

The root-mean-square error (RMSE) values for rotor lateral displacement during transient acceleration, and deceleration in the X-direction are 0.081 and 0.078, and in the Y-direction, they are 0.076 and 0.069, respectively. These RMSE values indicate a small discrepancy between the measured and predicted lateral rotor vibrations. Visual inspection of the figures confirms a close match between the overlapped signals. Furthermore, we conducted sensitivity analyses to assess the tolerance for RMSE errors. These analyses aimed to understand how variations in the SINDy model parameters and measurement conditions impact RMSE values. Specifically, we investigated the effects of increasing rotor imbalance parameters and adding Gaussian white noise to the signals as part of our sensitivity analysis of the SINDy model. In practice, an SNR of 20 dB or higher is often considered acceptable for many vibration analysis applications.

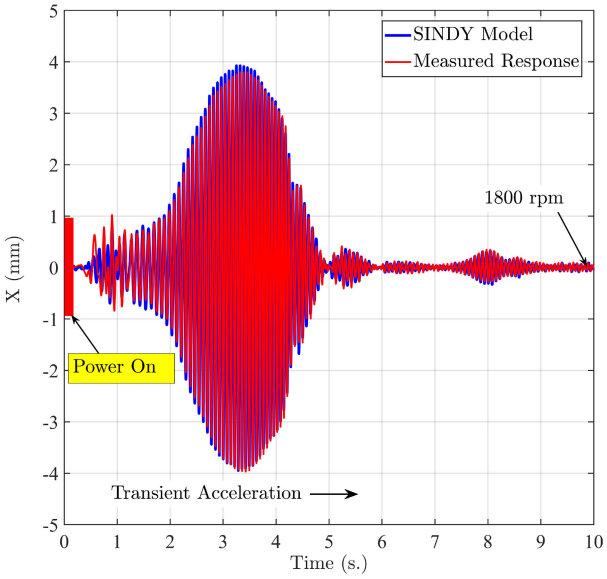

FIGURE 7. Comparing the SINDy-modeled lateral displacement of the rotor center with the measured data during acceleration in the X-axis.

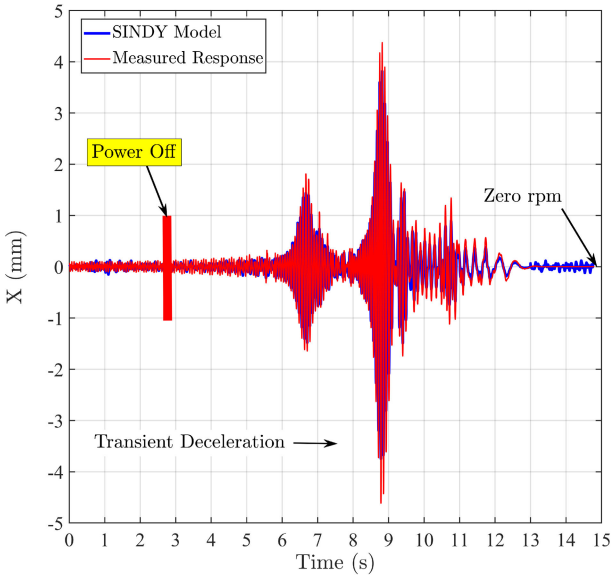

FIGURE 8. Comparing the SINDy-modeled lateral displacement of the rotor center with the measured data during deceleration in the X-axis.

To assess robustness in the presence of noise, a typical 20 dB measurement noise was introduced to recorded signals, and the SINDy model was employed to identify system parameters using these noisy measurements. Figures 9 and 10 show the X and Y components of the rotor's center in the presence of synthetic noise from the simulation and experiment. The corresponding RMSE values are listed in Table 2.

To investigate the accuracy and robustness of the SINDy-derived model, we examine the SINDy model during rotor shutdown (deceleration) for a balanced rotor and for two

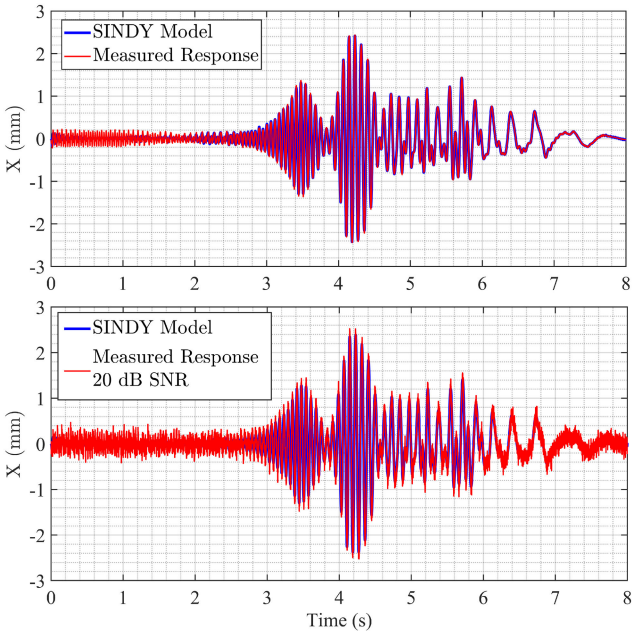

FIGURE 9. Comparing the SINDy model for rotor transient response with the addition of a typical 20 dB Gaussian white noise to measured data from a balanced rotor in the *X*-axis. Figures 9*a* (top) and 9*b* (bottom) illustrate SINDy results with and without noise in the *X*-axis.

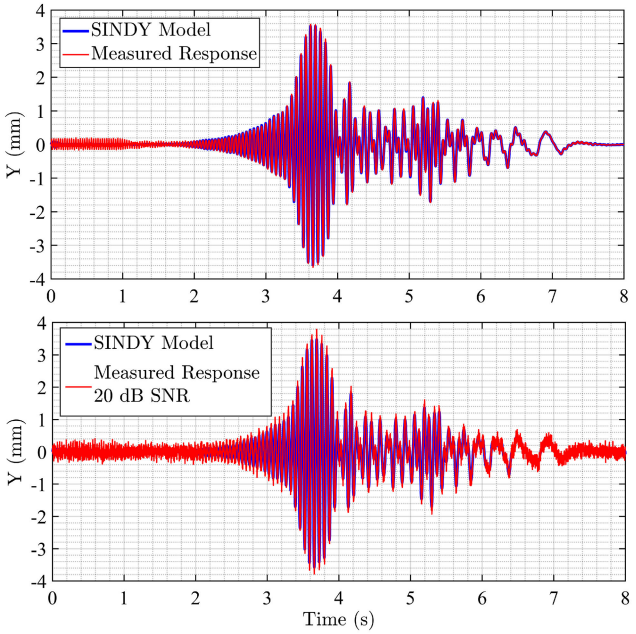

FIGURE 10. Comparing the SINDy model for rotor transient response with the addition of 20 dB Gaussian white noise to measured data from a balanced rotor in the *X*-axis. Figures 10*a* (top) and 10*b* (bottom) illustrate SINDy results with and without noise in the *Y*-axis.

additional scenarios involving 2.5 grams and 5.0 grams of induced imbalance loads.

Figures 11, 12, and 13 illustrate the comparison of the SINDy model with imbalanced-mass measurements. The corresponding RMSE values are presented in Table 2.

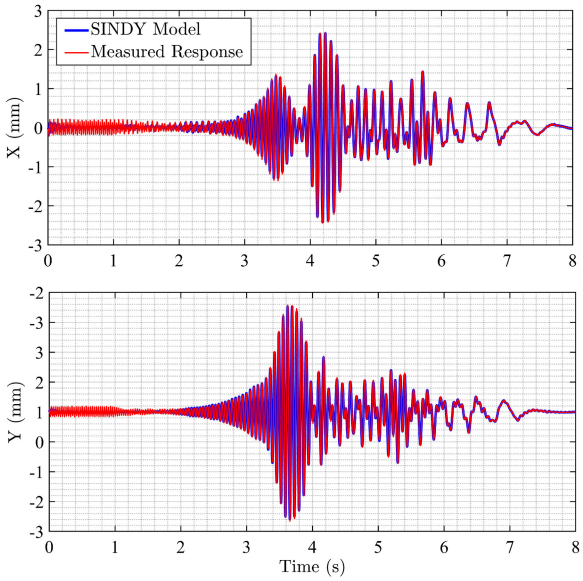

FIGURE 11. Comparison of SINDy model predictions for a balanced rotor during deceleration in the *X*-axis (top) and *Y*-axis (bottom).

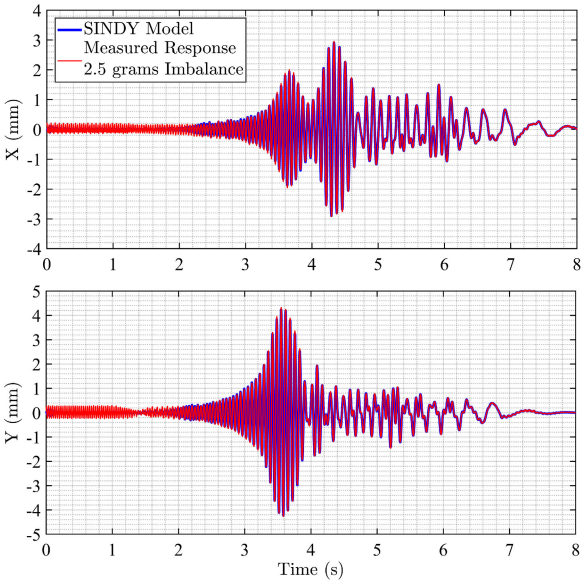

FIGURE 12. Comparison of SINDy model predictions for a balanced rotor during deceleration in the *X*-axis (top) and *Y*-axis (bottom) with an induced 2.5 grams imbalance.

After validating the derived data-driven model, the next step is to design an active vibration control law to mitigate the vibration.

VI. NONLINEAR CONTROLLER DESIGN BASED ON THE TSMC TECHNIQUE

Following the framework outlined in Figure 1, the control objective is to regulate the center of geometry position during the startup and shutdown modes of operation. To achieve this, we utilize the derived model and implement the terminal

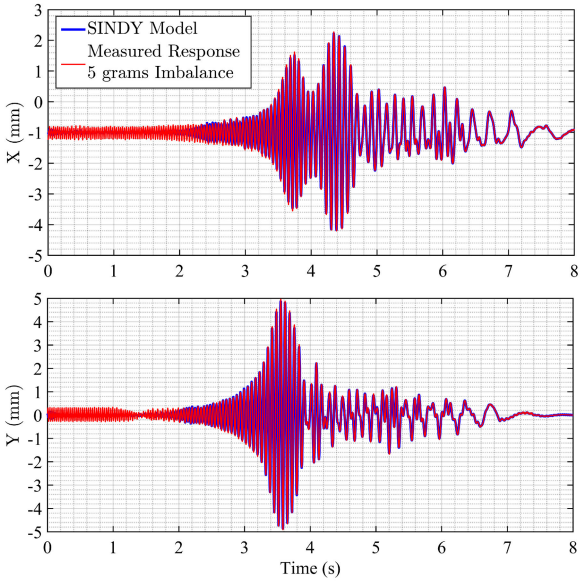

FIGURE 13. Comparison of SINDy model predictions for a balanced rotor during deceleration in the X-axis (top) and Y-axis (bottom) with an induced 5.0 grams imbalance.

TABLE 2. RMSE results of SINDy simulation versus actual measurement for noise and imbalance limits.

Figure No.	RMSE Value
9a	0.046
9b	0.128
10a	0.042
10b	0.111
11a	0.045
11b	0.046
12a	0.055
12b	0.076
13a	0.073
13b	0.082

sliding mode control technique, a robust nonlinear control method chosen to accomplish our goal.

In the following, we utilize the derived model, which is obtained offline, to design the control system. The system model can be rewritten as

$$\Sigma_{\text{SINDy}}: \begin{cases} \dot{X}_1 = X_2, \\ \dot{X}_2 = f_2(X,t) + \Delta_X + U_X, \\ \dot{X}_3 = X_4, \\ \dot{X}_4 = f_4(X,t) + \Delta_Y + U_Y, \\ \dot{X}_5 = X_6, \\ \dot{X}_6 = (1/\bar{J})(C_{m_1} + C_{m_2}X_6 \\ \qquad -C_cX_6 - C_aX_6\,|X_6| - C_vX_6), \end{cases} \tag{25}$$

where $f_2(X,t)$ and $f_4(X,t)$ functions are defined as

$$f_2(X,t) = \frac{1}{m}\Big\{ -K_1X_1 - K_2X_1^3 - C_1X_2 - K_2X_1X_3^2 + m\,e\Big[X_6^2\cos(X_5) + \frac{1}{\bar{J}}\Big(-C_c\text{sgn}(X_6) - C_vX_6 - C_aX_6|X_6|\Big)\sin(X_5)\Big] + f(X_6,t)\Big\},$$

$$f_4(X,t) = \frac{1}{m}\Big\{ -K_1X_3 - K_2X_3^3 - C_2X_4 - K_2X_1^2X_3 + m\,e\Big[X_6^2\sin(X_5) - \frac{1}{\bar{J}}\Big(-C_c\text{sgn}(X_6) - C_vX_6 - C_aX_6|X_6|\Big)\cos(X_5)\Big] + g(X_6,t)\Big\}, \tag{26}$$

and their coefficients are found by SINDy algorithm. The Δ_X, Δ_Y are uncertainty in the system with known upper bound, ρ_1 and ρ_2, i.e. $|\Delta_X| < \rho_1$ and $|\Delta_Y| < \rho_2$. The output of the system is the lateral displacement of the rotor center (x, y), and $U_X \in \mathbb{R}$ and $U_Y \in \mathbb{R}$ are control inputs as shown in Figure 2. For such system, we consider two classical TSMC manifolds [41], [42], [43], [44] acting in perpendicular directions to X- and Y-axes of the form:

$$S_x = X_2 + \mathcal{C}_1\,|X_1|^{(\frac{q}{p})}\,\text{sgn}(X_1),$$
$$S_y = X_4 + \mathcal{C}_2|X_3|^{(\frac{q}{p})}\,\text{sgn}(X_3). \tag{27}$$

The parameters p and q are positive odd integers, with $p > q$. The condition $p > q$ ensures that the convergence to the sliding surface is faster than linear, providing the necessary nonlinearity to ensure finite-time convergence. The sgn(.) function is the signum function. The coefficients $\mathcal{C}_1$ and $\mathcal{C}_2$, belonging to $\mathbb{R}^+$, serve as design parameters and will be adjusted during the fine-tuning process of the controller to achieve optimal output performance. The manifold ensures that when the system states X_1 and X_3 reach the sliding surface $S = 0$, the system will converge to the equilibrium point $X_1, X_3 = 0$ in finite time.

To find a control law that guarantees the stability of the closed-loop system, we apply the Lyapunov stability theorem and choose a quadratic candidate Lyapunov function in the form of

$$V(X) = \frac{1}{2}S^TS, \tag{28}$$

where $S = [S_x,\ S_y]^T$, $V(0) = 0$, and the Lyapunov function is positive definite in the region around the equilibrium point except at the origin, i.e. $V(x) > 0$.

States X_5 and X_6 are associated with the angular displacement and angular velocity of the rotor during its transient motion. In our research, during both the acceleration and deceleration phases of the rotor, the AC motor is equipped with a separate speed controller that applies a constant angular acceleration to the rotor $\ddot{\beta}(t) = \text{constant} \in \mathbb{R}$. When the angular acceleration remains constant, both $X_5 = \beta(t)$ and $X_6 = \dot{\beta}(t)$ become explicit functions of time. The structure of the Lyapunov function $V(X) = V(X_1, X_2, X_3, X_4)$ is based on the internal states of the system acting in planar motion of the rotor which is sufficient to ensure the stability of the closed-loop system.

The control law should satisfy the reaching condition,

$$S\dot{S} \le -\eta_1|S_x| - \eta_2|S_y|,\ \eta_1 > 0,\ \eta_2 > 0, \tag{29}$$

and reach the sliding surface $S_x = S_y = 0$ in a finite-time [42]:

$$t_{reach} = \frac{1}{\mathcal{C}_1}\left(1-\frac{q}{p}\right)^{-1}|x(0)|^{1-(\frac{q}{p})}, \tag{30}$$

where $X(0)$ is the initial condition. The time derivative of $V(X)$ can be found from

$$\dot{V}(X) = S_x\dot{S}_x + S_y\dot{S}_y. \tag{31}$$

To this end,

$$\begin{aligned}\dot{S}_x &= \dot{X}_2 + \mathcal{C}_1\left(\frac{q}{p}\right)|X_1|^{\left(\frac{q}{p}\right)-1}X_2,\\ \dot{S}_y &= \dot{X}_4 + \mathcal{C}_2\left(\frac{q}{p}\right)|X_3|^{\left(\frac{q}{p}\right)-1}X_4.\end{aligned} \tag{32}$$

Then by enforcing the condition, $\dot{V}(X) < 0$, we can write,

$$\begin{aligned}\dot{V}(X) = S_x\Big[\dot{X}_2 + \mathcal{C}_1\big(\frac{q}{p}\big)|X_1|^{(\frac{q}{p})-1}X_2\Big]\\ + S_y\Big[\dot{X}_4 + \mathcal{C}_2\big(\frac{q}{p}\big)|X_3|^{(\frac{q}{p})-1}X_4\Big] < 0,\end{aligned} \tag{33}$$

and substituting $\dot{X}_2$ and $\dot{X}_4$ from (25), (33) can be rewritten as follows:

$$\begin{aligned}\dot{V}(X) = S_x\Big[f_2(X,t) + \Delta_X + U_X\\ + \mathcal{C}_1\big(\frac{q}{p}\big)|X_1|^{(\frac{q}{p})-1}X_2\Big]\\ + S_y\Big[f_4(X,t) + \Delta_Y + U_Y\\ + \mathcal{C}_2\big(\frac{q}{p}\big)|X_3|^{(\frac{q}{p})-1}X_4\Big] < 0.\end{aligned} \tag{34}$$

The control signal $U = [U_X, U_Y]^T$ has two parts in each X-axis and Y-axis, respectively, as follows:

$$U = [U_{Xn} + U_{Xr},\ U_{Yn} + U_{Yr}]^T, \tag{35}$$

where $U_{Xn}, U_{Yn} \in \mathbb{R}$ are part of the control signal that cancels the nominal part of the SINDy nonlinear function, and $U_{Xr}, U_{Yr} \in \mathbb{R}$ are the terms that guarantee the robustness of the controller in the presence of Δ_X and Δ_Y for the unidentified dynamics related to the disturbance. We can separate the control vector U as follows:

$$\begin{aligned}U_{Xn} &= -f_2(X,t) - \mathcal{C}_1\left(\frac{q}{p}\right)|X_1|^{\left(\frac{q}{p}\right)-1}X_2,\\ U_{Yn} &= -f_4(X,t) - \mathcal{C}_2\left(\frac{q}{p}\right)|X_3|^{\left(\frac{q}{p}\right)-1}X_4.\end{aligned} \tag{36}$$

After substituting (36) into (34), we can write:

$$\dot{V}(X) = S_x\big(\Delta_X + U_{Xr}\big) + S_y\big(\Delta_Y + U_{Yr}\big) < 0. \tag{37}$$

The positive constants κ_1, κ_2 are chosen such that they satisfy

$$\begin{aligned}S_x\big(\Delta_X + U_{Xr}\big) \le -\kappa_1|S_x|,\\ S_y\big(\Delta_Y + U_{Yr}\big) \le -\kappa_2|S_y|.\end{aligned} \tag{38}$$

then (37) can be simplified as

$$\dot{V}(X) \le -\kappa_1|S_x| - \kappa_2|S_y|. \tag{39}$$

The U_{Xr}, U_{Yr} part of control laws can be chosen as

$$\begin{aligned}U_{Xr} &= -\rho_1\ \mathrm{sgn}(S_x),\\ U_{Yr} &= -\rho_2\ \mathrm{sgn}(S_y).\end{aligned} \tag{40}$$

When S is positive (i.e., the system state is on one side of the sliding surface), the signum function returns 1. In this case, the control input U will be negative and proportional to the magnitude of S. The larger the positive value of S, the more negative and stronger the control input U will be. When S is negative (i.e., the system state is on the other side of the sliding surface), the signum function returns -1. In this case, the control input U will be positive and proportional to the magnitude of S. The larger the negative value of S, the more positive and stronger the control input U will be. When S is exactly zero, the signum function returns 0, indicating no control input. This means that when the system state is exactly on the sliding surface (i.e., the desired behavior is achieved), there is no control action.

Using the absolute values of the left-side terms in (38), we can further reduce and bound the range of the inequality constraint. It can be expressed as follows:

$$\begin{aligned}|S_x|\ |\Delta_X| - \rho_1|S_x| \le -\kappa_1|S_x|,\\ |S_y|\ |\Delta_Y| - \rho_2|S_y| \le -\kappa_2|S_y|.\end{aligned} \tag{41}$$

Since we assumed $|\Delta_X| < \rho_1$ and $|\Delta_Y| < \rho_2$, then we can write the inequality as

$$\begin{aligned}\rho_1 > |\Delta_X| + \kappa_1,\\ \rho_2 > |\Delta_Y| + \kappa_2,\end{aligned} \tag{42}$$

where ρ_1, ρ_2 are design tuning parameters. In order to reduce the chattering in the control law, we replace the sgn(S) with tanh (S/ϵ) function in which ϵ is a small positive number.

Substituting (40) and (36) into (35), the TSMC law can be written as

$$\begin{aligned}U_X &= -\left[f_2 + \mathcal{C}_1\left(\frac{q}{p}\right)|X_1|^{(\frac{q}{p}-1)}X_2 + \rho_1\ \tanh\left(\frac{S_x}{\epsilon}\right)\right],\\ U_Y &= -\left[f_4 + \mathcal{C}_2\left(\frac{q}{p}\right)|X_3|^{(\frac{q}{p}-1)}X_4 + \rho_2\ \tanh\left(\frac{S_y}{\epsilon}\right)\right].\end{aligned} \tag{43}$$

The control laws derived in Equation (43) represent the TSMC control law applied to the rotary system dynamics in the X and Y directions.

VII. EXPERIMENTAL RESULTS

A. DESCRIPTION OF THE LABORATORY-SCALE ROTARY SYSTEM

To validate the proposed SINDY-TSMC active vibration control, we designed a test rig that incorporates a disc-shaped rotor with multiple apertures designed to accommodate weights. These apertures allow for the intentional

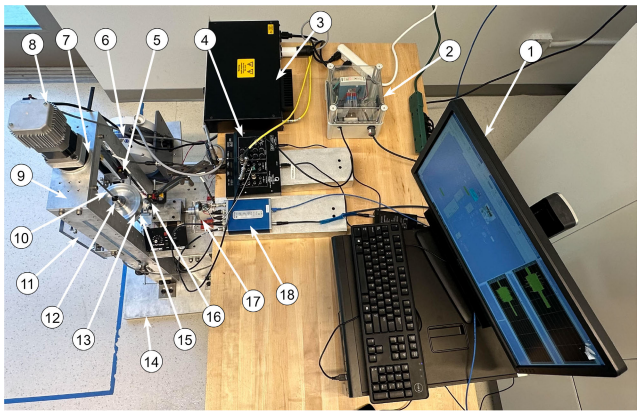

FIGURE 14. The image illustrates the mechanical and hardware assembly of the test-rig system, showcasing the actuators and sensors in the *X*- and *Y*-axes, along with the rotor chassis assembly.

displacement of the rotor from its geometric center. This displacement is a key feature that amplifies the vibration dynamics under investigation shown as the mass eccentricity parameter e in Figure 2. Figures 14 and 15 show the test rig assembly and its components. The system is driven by a variable-frequency AC electric motor, coupled with a gearbox and a damping plate, to effectively regulate and control the rotation speed. During operational phases, a linear speed profile is employed to initiate and conclude rotary system operations, ensuring consistent acceleration during startup and uniform deceleration during shutdown, where $\ddot{\beta} = c$ and $c \in \mathbb{R}$ is a constant. This approach effectively manages vibrations in scenarios where rotor angular velocity exhibits time-dependent behavior, thereby enhancing the operational stability and reliability of rotary systems. To transmit the torque from the motor to the system, a 6 mm steel shaft is employed, connected to the damping plate via Lovejoy® couplings. These couplings are selected for their excellent shock absorption properties and tolerance for shaft misalignment.

To ensure unrestricted planar disc vibrations, a centrifugal clutch mechanism is introduced to couple the rotor and shaft. This mechanism effectively nullifies any misalignment that may arise from manufacturing tolerances, ensuring precise and consistent performance. The test rig itself is securely mounted on an aluminum chassis, which provides standardized screw mounting points for the placement of sensors and actuators. This design ensures the stability and versatility of the test setup, making it a robust platform for conducting experiments and validating the proposed control system. Table 3 describes each component used in the active vibration control system and the assembly. The hardware diagram of the system is shown in Figure 16. We utilized Micro-Epsilon non-contact opto-NCDT-1420 laser displacement sensors with a measuring rate of 4 *kHz*. These sensors, equipped with an RS422 interface and powered by 24 *volts*, introduce no additional mass to the system. Control is facilitated through a Quanser Q8 DAQ control board,

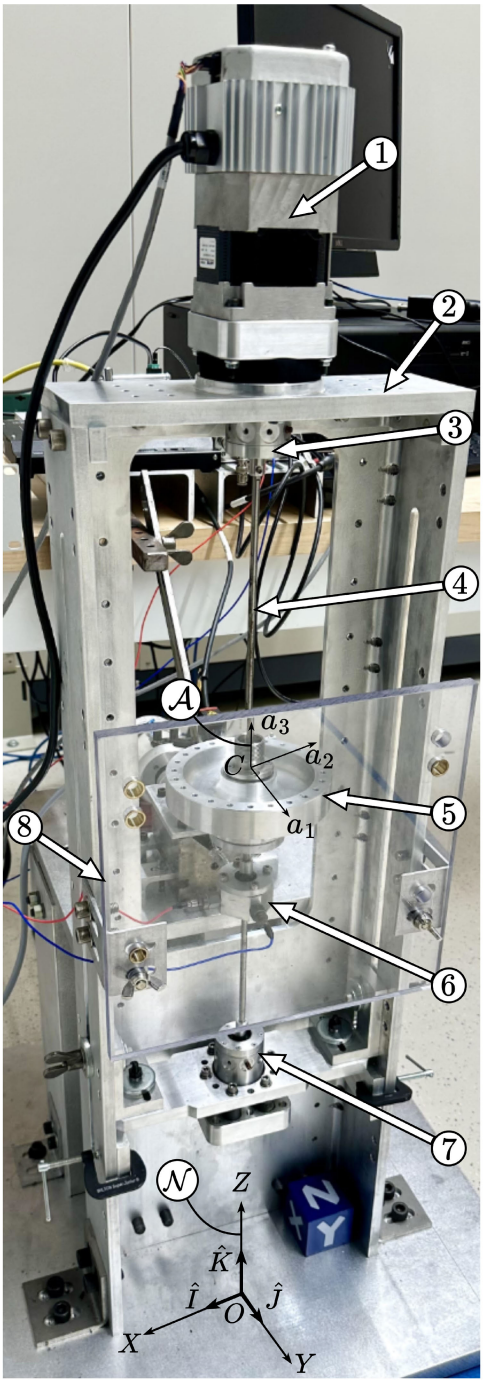

FIGURE 15. The image displays the front view mechanical assembly of the rotor chassis components of the rotary test rig. An AC motor ① is mounted on the chassis ② and applies torque to the drive system mechanism involving the disk rotor ⑤, which is mounted on a slender, flexible shaft ④. This shaft extends through the rotor and connects to the actuator force transmission assembly, which, in turn, is connected to the rotor bearing ⑥. Subsequently, this assembly is linked to the bearing housing at the top ③ and at the bottom ⑦. A safety shield ⑧ covers the front panel.

enabling real-time control via MATLAB® and Simulink®. We tested the proposed control law and found that the computations are real-time-friendly, with a processing time

TABLE 3. Hardware components of the rotary test rig for evaluation of SINDY-TSMC control system shown in Figure 14.

label	Description
1	Computer/Monitor
2	RS422 interface and 24V adapter
3	Amplifier
4	Quanser Q8 DAQ
5	Y-axis Laser position sensor optoNCDT 1420
6	Y-axis Actuator
7	Cylindrical rubber damper, coupling, and Bearing housing
8	Variable speed AC motor
9	C-channel mounting chassis
10	6 mm diameter steel drive shaft
11	Safety shield
12	Centrifugal clutch
13	Disk Rotor
14	Base mounting plate
15	X-axis and Y-axis accelerometer sensors and actuators mounting adapter
16	X-axis Laser position sensor optoNCDT 1420
17	X-axis Actuator
18	Spider-20 DAQ and EDM system

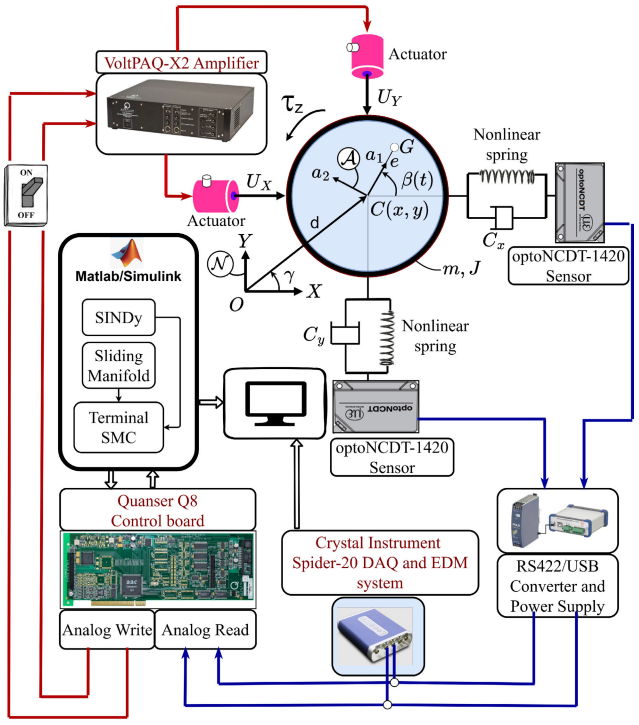

FIGURE 16. Hardware diagram for the SINDY-TSMC: The blue lines represent signals originating from sensors and processed through Spider-20 DAQ/EDM and Quanser analog reading. These signals then pass through Matlab for SINDY-TSMC to generate control signals. The red lines represent controlled signals, transferred to Quanser, and subsequently transmitted via analog write to actuators. These actuators apply control forces to the rotor. Blue lines correspond to measured signals, while red lines denote controlled signals in the system.

of less than 1 ms on the Quanser board. The resolution of the control board is 16-bit. Additionally, the input range for both the input and the output analog voltage is ±10 V. The QUARC^{TM} software converts Simulink-designed controller code into real-time C code executed on Windows. The laser sensor voltage signals are translated into control signals through analog channels and then sent via analog-write channels to the VoltPAQ-X2 amplifier. These signals exert mechanical force through actuators on the rotor drive bearing beneath the rotor's center, as depicted in Figure 2. Additionally, the Crystal Instrument Spider-20 Dynamic Signal Analyzer captures sensor signals, as illustrated in Figure 16. Using Crystal Instruments Engineering Data Management (EDM) software, the controller's performance is independently monitored. EDM's real-time display reveals the application of the control law's desired force on the rotor, providing convenient online vibration monitoring in both time and frequency domains with recording capabilities.

B. REAL-TIME EXPERIMENTAL RESULTS

Figure 17 shows the computer simulation result of the closed-loop control system during deceleration. The initial condition at the start of control is marked as ①, and the vibration error reaches a finite-time state at ② is 0.55 s. The specific time required for the system to reach the sliding surface in TSMC can vary based on factors such as control design, system dynamics, and initial conditions. Finite-time stability is crucial in a rotary system where quick and robust convergence to the desired state is imperative. After that, the response remains in the small boundary layer around the sliding manifold.

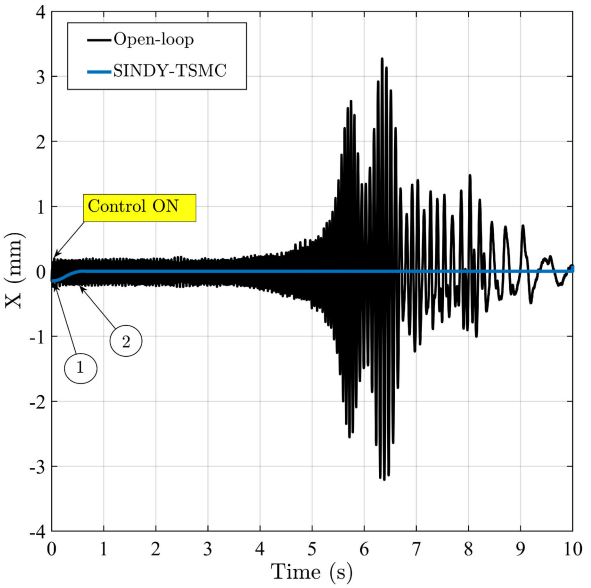

FIGURE 17. Comparing the closed-loop simulation and measured data (open-loop) during the deceleration.

Figure 18 presents a comparison between the measured responses of a balanced rotor in both time and frequency domains under two control strategies during transient response: a Proportional-Derivative (PD) controller, a standard technique widely used in various industrial applications, and the proposed SINDY-TSMC controller. In PD control,

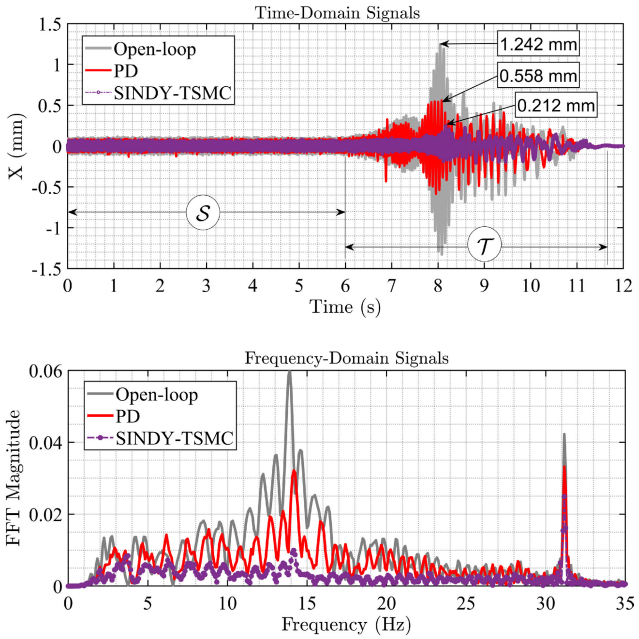

FIGURE 18. Comparison of open-loop versus closed-loop transient responses Between PD and SINDY-TSMC controllers for a balanced rotor.

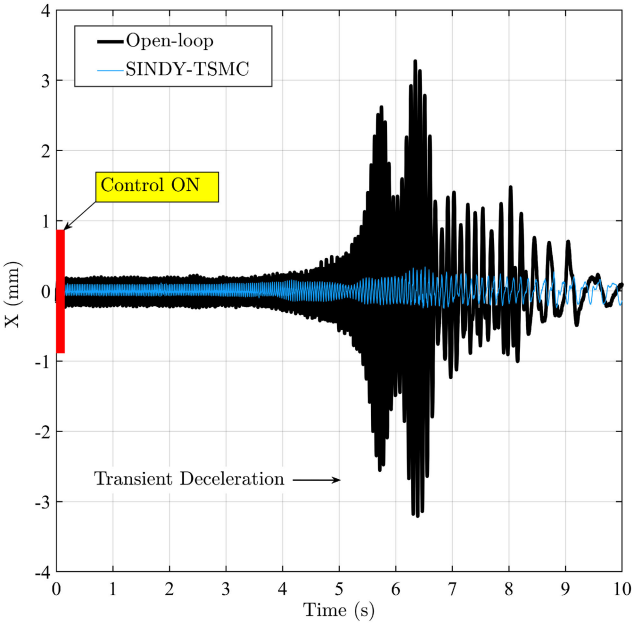

FIGURE 19. Comparing the measured and closed-loop response of the rotor with a 5.0 *gram* mass imbalance in the *X*-axis direction.

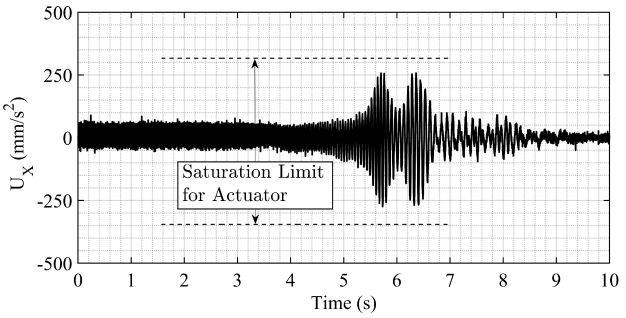

FIGURE 20. The control signal U_X utilized for controlling the transient response shown in Figure 19.

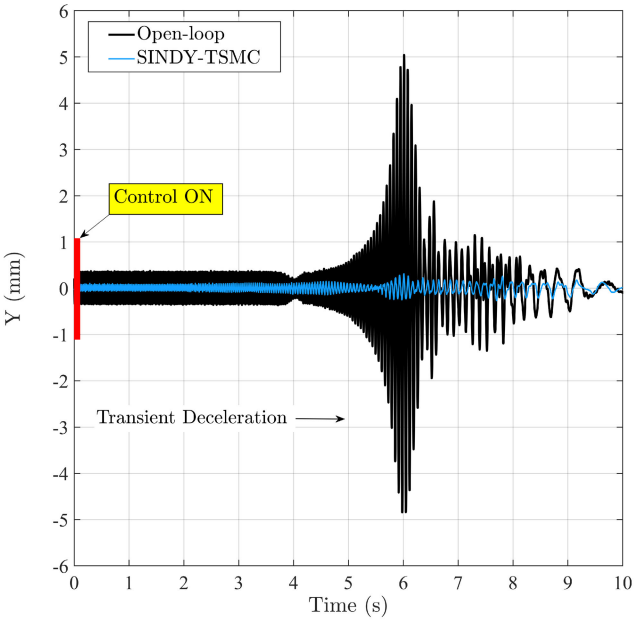

FIGURE 21. Comparing the measured and closed-loop response of the rotor with a 5.0 gram mass imbalance in the *Y*-axis direction.

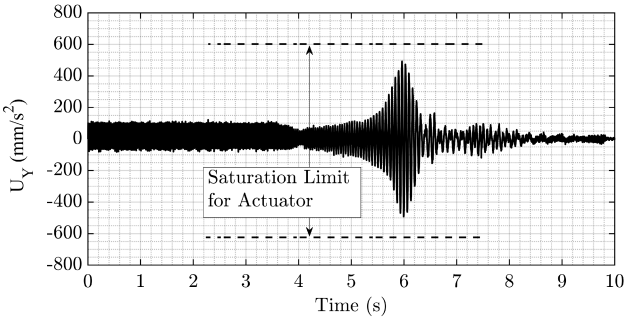

FIGURE 22. The control signal U_Y utilized for controlling the transient response shown in Figure 21.

the proportional term reacts to the current error between the desired setpoint and the actual output, generating a control action proportional to the error, while the derivative term anticipates future trends to dampen oscillations and enhance system stability. Although PD control effectively handles real-time error responses, it lacks robustness in managing rapid variable frequency in rotor transient responses and the nonlinearities dominant in rotordynamic systems. Conversely, SINDY-TSMC represents an advanced nonlinear technique tailored for such complex systems. We tuned the PD gains K_p and K_d through a comprehensive trial-and-error process to obtain the best possible performance. Then, we adjusted the parameters of SINDY-TSMC, such

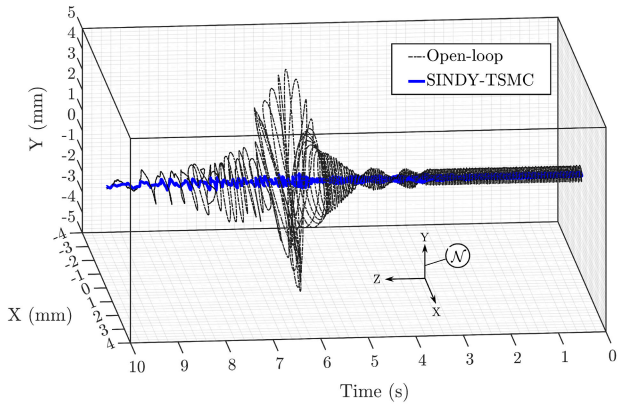

FIGURE 23. The three-dimensional response of the closed-loop vibration control and measured data during deceleration with a 5.0 grams mass imbalance.

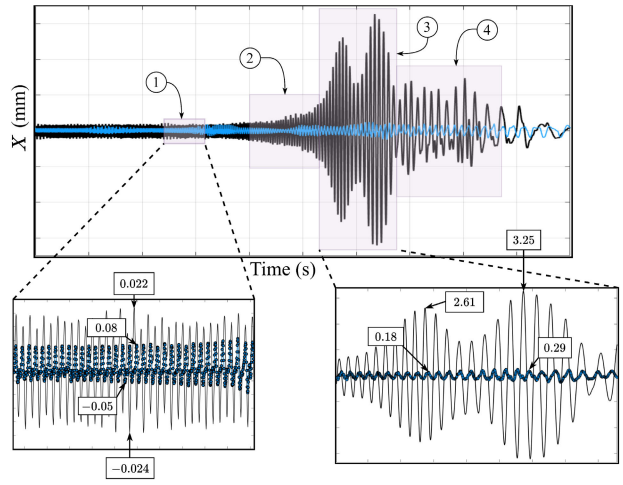

FIGURE 24. The replication of Figure 19 illustrates the transient curve, providing comprehensive details about the response of four segments along the *X*-axis direction in both steady-state and transient modes. This information is particularly relevant to the principal frequency of the system, showcasing the performance of TSMC active vibration control in this region. Segment ① reflects the stability of the phase diagram before the system reaches its principal frequencies. Segment ② is associated with control results as the rotor enters the critical region, while segment ③ presents control outcomes as the rotor passes through the principal frequencies. Segment ④ pertains to the end of the control process when the rotor comes to a stop. The measured data are in *mm – Peak* and show the amplitude of each segment.

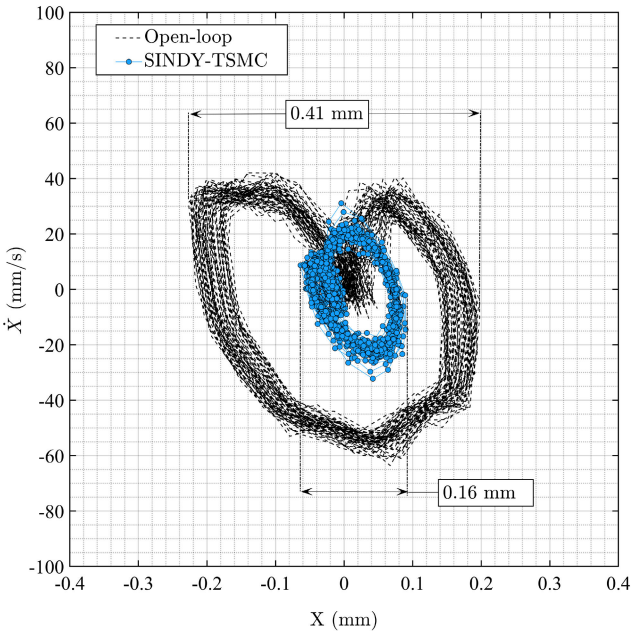

FIGURE 25. The phase-plane diagram of segment ①.

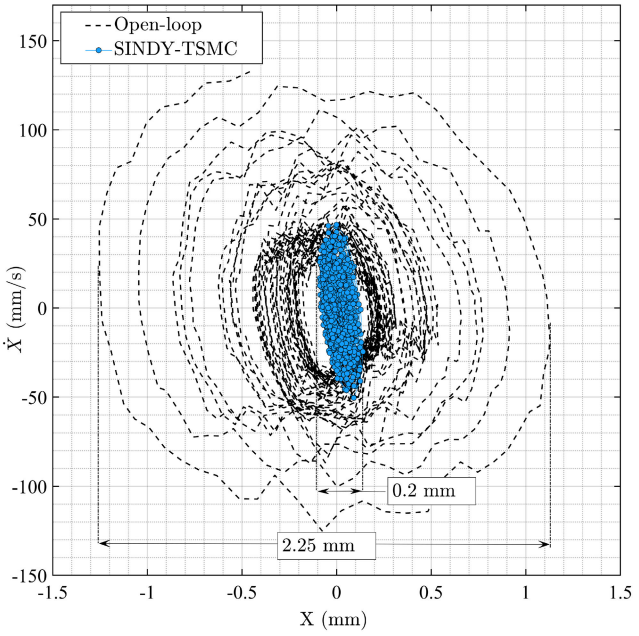

FIGURE 26. The phase-plane diagram of segment ②.

as the C, ρ, p, and q controllers, to closely match the initial performance of the PD controller, as shown in the region $\mathcal{S}$ representing steady-state conditions. While PD control significantly improves vibration, it cannot achieve the performance level of SINDY-TSMC, as evident from the measured response shown in regions $\mathcal{T}$ representing transient response conditions. Quantitatively, the effectiveness of vibration suppression can be compared by measuring the peak amplitudes of the original measured signal in open-loop and the tuned closed-loop controlled signals. In this case, the peak amplitude of the open-loop signal is measured to be 1.242 mm. With the PD controller, vibration suppression in closed-loop at the highest peak reaches 0.558 mm, whereas the SINDY-TSMC controller, even at comparable tuning levels, achieves 0.212 mm of suppression. This difference in suppression percentages further underscores the superior performance of the SINDY-TSMC controller in mitigating vibrations of rotary systems. The percentage of vibration suppression for the PD controller remains approximately 55.1%, compared to approximately 82.9% for the SINDY-TSMC controller.

Next, the real-time simulation of the SINDY-TSMC control system is evaluated using the hardware described

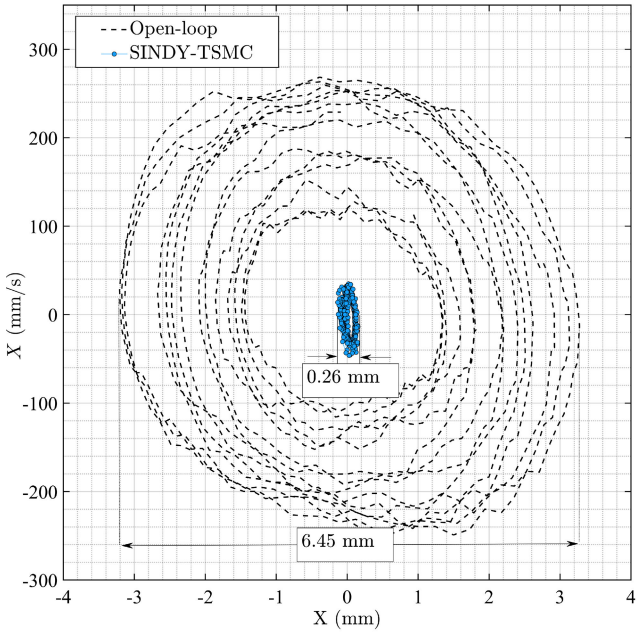

FIGURE 27. The Phase-plane diagram of segment ③. This segment demonstrates a remarkable vibration suppression of 96% during the rotor's transition through the natural frequency of the system.

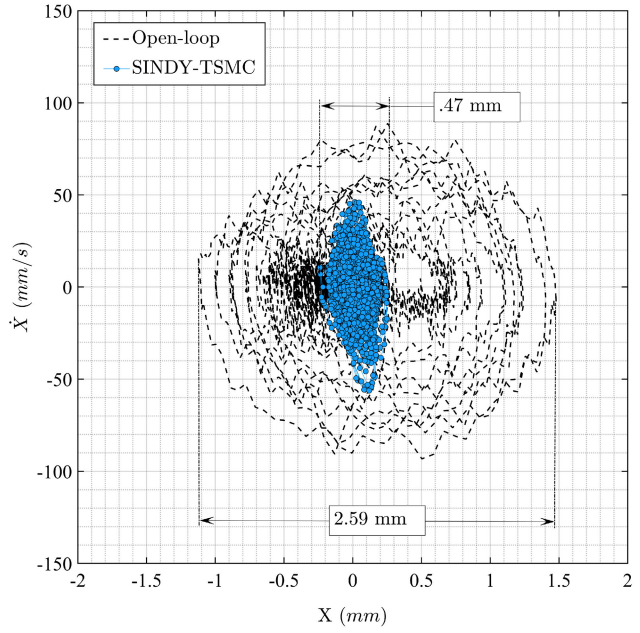

FIGURE 28. The phase-plane diagram of segment ④.

in Figure 16. The test results for the closed-loop system and the control signal in X-axis are presented in Figures 19 and 20 while the test results for the closed-loop system and the control signal in Y-axis are shown in Figures 21 and 22.

Figure 23 presents a three-dimensional view of the rotor center motion versus time during transient deceleration. This motion, characterized by deviations from an ideal circular path, is influenced by a 5.0 grams mass imbalance and involves the rotor passing through the system's natural frequencies in a nonlinear pattern. When the rotor's rotational speed approaches the natural frequency of the system, resonance occurs, resulting in amplified vibrations. The uncontrolled motion of the rotor follows a gradually increasing funnel shape, as seen in the figure. Figure 24 shows the details of Figure 19. It can be seen that the SINDY-TSMC suppresses the lateral transient vibration at the maximum peak corresponding to the principal natural frequency of the system and reduces the peak vibration in segment ③ from 3.25 mm to below 0.17 mm. The peak value of the response and the percent of vibration suppression are listed in Table 4.

TABLE 4. Numerical results of vibration peaks (mm) for the open-loop and closed-loop active vibration control during rotor deceleration.

Segment	Open-loop	SINDY-TSMC	Vibration suppression (%)
1	0.41	0.16	61
2	2.25	0.2	91
3	6.45	0.26	96
4	2.59	0.47	81.8
5	6.45	0.47	92.7

The phase-plane diagrams showcase the control's impact on vibration suppression during transient responses and are presented in Figures 25–28. Overall, this experimental study demonstrates the effectiveness of the SINDY-TSMC control strategy in actively controlling lateral transient vibrations in a rotor system.

VIII. CONCLUSION

This paper presents a physics-based data-driven approach utilizing SINDy and experimental data to reconstruct the nonlinear differential equations of a vertical-shaft rotary machine. Following model validation, we designed a robust nonlinear vibration suppression controller employing the TSMC technique. Comparative evaluations with a standard PD controller underscored the advantages of the SINDY-TSMC in managing control errors near system resonance, resulting in a robust control system tailored to transient responses of rotary systems. Real-time tests validated the proposed control system, demonstrating its efficacy in reducing vibrations on a laboratory-scale rotary system. These findings emphasize the potential applications of the combined physics-based, data-driven modeling and terminal sliding mode control technique, enhancing the performance of vertical shaft rotary systems. In the future, we plan to investigate the efficacy of learning-control techniques, such as reinforcement learning, and compare the results with our physics-informed, data-driven approach. Additionally, we intend to implement our approach on a standard industrial centrifugal machine to delve into practical challenges and

refine our approach for the next generation of high-performance centrifugal machines.

REFERENCES

[1] S. Markidis. (2021). *Physics-Informed Deep-Learning for Scientific Computing*. [Online]. Available: https://api.semanticscholar.org/CorpusID:232257802

[2] S. L. Brunton and J. N. Kutz, *Data-Driven Science and Engineering: Machine Learning, Dynamical Systems, and Control*. Cambridge, U.K.: Cambridge Univ. Press, 2019.

[3] F. Lejarza and M. Baldea, "Data-driven discovery of the governing equations of dynamical systems via moving horizon optimization," *Sci. Rep.*, vol. 12, no. 1, Jul. 2022, Art. no. 11836, doi: 10.1038/s41598-022-13644-w.

[4] E. Kaiser, J. N. Kutz, and S. L. Brunton, "Sparse identification of nonlinear dynamics for model predictive control in the low-data limit," *Proc. Roy. Soc. A, Math., Phys. Eng. Sci.*, vol. 474, no. 2219, Nov. 2018, Art. no. 20180335, doi: 10.1098/rspa.2018.0335.

[5] L. Walha, Ed., *Design and Modeling of Mechanical Systems—V: Proceedings of the 9th Conference on Design and Modeling of Mechanical Systems, CMSM'2021, December 20-22, 2021, Hammamet, Tunisia* (Lecture Notes in Mechanical Engineering). Switzerland: Springer, Aug. 2022.

[6] C. Du and L. Xie, *Modeling and Control of Vibration in Mechanical Systems*, 1st ed., Boca Raton, FL, USA: CRC Press, 2010.

[7] W. J. Chen and E. J. Gunter, *Introduction to Dynamics of Rotor-Bearing Systems*. Bloomington, IN, USA: Trafford Publishing, 2005.

[8] M. Friswell, J. Penny, S. Garvey, and A. Lees, *Dynamics of Rotating Machines*. New York, NY, USA: Cambridge Univ. Press, 2010, doi: 10.1017/cbo9780511780509.

[9] S. Hamzehlouia and K. Behdinan, "A study of lubricant inertia effects for squeeze film dampers incorporated into high-speed turbomachinery," *Lubricants*, vol. 5, no. 4, p. 43, Oct. 2017, doi: 10.3390/lubricants5040043.

[10] R. Walker, S. Perinpanayagam, and I. K. Jennions, "Rotordynamic faults: Recent advances in diagnosis and prognosis," *Int. J. Rotating Machinery*, vol. 2013, pp. 1–12, Feb. 2013, doi: 10.1155/2013/856865.

[11] Y. Ishida and T. Yamamoto, *Linear and Nonlinear Rotordynamics: A Modern Treatment With Applications*. Hoboken, NJ, USA: Wiley, 2012, doi: 10.1002/9783527651894.

[12] S. Piramoon, "System and method for balancing a centrifuge rotor," Patent 4 100 167 B1, Jan. 15, 2023. [Online]. Available: https://www.epo.org

[13] C. Fu, Y. Xu, Y. Yang, K. Lu, F. Gu, and A. Ball, "Response analysis of an accelerating unbalanced rotating system with both random and interval variables," *J. Sound Vib.*, vol. 466, Feb. 2020, Art. no. 115047, doi: 10.1016/j.jsv.2019.115047.

[14] M. Cheng, G. Meng, and B. Wu, "Nonlinear dynamics of a rotor-ball bearing system with Alford force," *J. Vib. Control*, vol. 18, no. 1, pp. 17–27, Jan. 2012, doi: 10.1177/1077546311405701.

[15] T. Ishibashi, B. Han, and T. Kawai, "Rotating machinery library for diagnosis," in *Proc. Linköping Electron. Conf.*, Jul. 2017, pp. 381–387, doi: 10.3384/ecp17132381.

[16] Y. Xia, X. Ren, W. Qin, Y. Yang, K. Lu, and C. Fu, "Investigation on the transient response of a speed-varying rotor with sudden unbalance and its application in the unbalance identification," *J. Low Freq. Noise, Vib. Act. Control*, vol. 39, no. 4, pp. 1065–1086, Dec. 2020, doi: 10.1177/1461348419861837.

[17] L. Cui and J. Zheng, "Nonlinear vibration and stability analysis of a flexible rotor supported on angular contact ball bearings," *J. Vib. Control*, vol. 20, no. 12, pp. 1767–1782, Sep. 2014, doi: 10.1177/1077546312474679.

[18] Z. Nasiri-Gheidari, F. Tootoonchian, and F. Zare, "Design oriented technique for mitigating position error due to shaft run-out in sinusoidal-rotor variable reluctance resolvers," *IET Electr. Power Appl.*, vol. 11, no. 1, pp. 132–141, Jan. 2017, doi: 10.1049/iet-epa.2016.0316.

[19] R. G. Kirk and E. J. Gunter, "The effect of support flexibility and damping on the synchronous response of a single-mass flexible rotor," *J. Eng. Ind.*, vol. 94, no. 1, pp. 221–232, Feb. 1972, doi: 10.1115/1.3428115.

[20] J. Zou, J. Chen, J. C. Niu, and Z. M. Geng, "Study on the transient response and wavelet time—Frequency feature of a cracked rotor passage through a subcritical speed," *J. Strain Anal. Eng. Design*, vol. 38, no. 3, pp. 269–276, Apr. 2003, doi: 10.1243/030932403765310590.

[21] Y. Ishida and T. Inoue, "Vibration suppression of nonlinear rotor systems using a dynamic damper," *J. Vib. Control*, vol. 13, no. 8, pp. 1127–1143, Aug. 2007, doi: 10.1177/1077546307074577.

[22] J. Huang and A. C. J. Luo, "Periodic motions and bifurcation trees in a buckled, nonlinear Jeffcott rotor system," *Int. J. Bifurcation Chaos*, vol. 25, no. 1, Jan. 2015, Art. no. 1550002, doi: 10.1142/s0218127415500029.

[23] M. Eissa and N. Saeed, "Nonlinear vibration control of a horizontally supported Jeffcott-rotor system," *J. Vib. Control*, vol. 24, no. 24, pp. 5898–5921, Dec. 2018, doi: 10.1177/1077546317693928.

[24] T. Wei, W. Gou, C. Fu, and Y. Yang, "Transient analysis of speed-varying rotor with uncertainty based on interval approaches," *Discrete Dyn. Nature Soc.*, vol. 2018, pp. 1–10, Jul. 2018, doi: 10.1155/2018/5904724.

[25] Q. Xu, J. Niu, H. Yao, L. Zhao, and B. Wen, "Nonlinear dynamic behavior and stability of a rotor/seal system with the dynamic vibration absorber," *Adv. Mech. Eng.*, vol. 11, no. 1, Jan. 2019, Art. no. 168781401881957, doi: 10.1177/1687814018819578.

[26] S. L. Brunton, J. L. Proctor, and J. N. Kutz, "Sparse identification of nonlinear dynamics with control (SINDYc)," *IFAC-PapersOnLine*, vol. 49, no. 18, pp. 710–715, 2016, doi: 10.1016/j.ifacol.2016.10.249.

[27] S. L. Brunton, J. L. Proctor, and J. N. Kutz, "Discovering governing equations from data by sparse identification of nonlinear dynamical systems," *Proc. Nat. Acad. Sci. USA*, vol. 113, no. 15, pp. 3932–3937, Apr. 2016, doi: 10.1073/pnas.1517384113.

[28] U. Fasel, E. Kaiser, J. N. Kutz, B. W. Brunton, and S. L. Brunton, "SINDy with control: A tutorial," *J. Mach. Learn. Res.*, vol. 22, no. 48, pp. 1–31, 2021.

[29] J. Xu, Y. Zhao, Z. Xu, and B. Zhang, "Active balancing control for time-delay rotor via linear-quadratic regulator," *Proc. SPIE*, vol. 30, no. 3, Jan. 2021, Art. no. 031205, doi: 10.1117/1.jei.30.3.031205.

[30] L. Zhang, L. Luo, and J. Xu, "An improved adaptive control method for active balancing control of rotor with time-delay," *IEICE Electron. Exp.*, vol. 14, no. 23, 2017, Art. no. 20171069, doi: 10.1587/elex.14.20171069.

[31] M. Mohebbi and M. Hashemi, "Reducing the vibrations of an unbalanced rotary engine by active force control," *Int. J. Technol.*, vol. 7, no. 1, p. 141, Jan. 2016. [Online]. Available: https://ijtech.eng.ui.ac.id/article/view/1532

[32] K. Chen, Z. Li, W.-C. Tai, K. Wu, and Y. Wang, "MPC-based vibration control and energy harvesting using an electromagnetic vibration absorber with inertia nonlinearity," 2020, *arXiv:2005.05728*.

[33] J.-N. Juang and R. S. Pappa, "An eigensystem realization algorithm for modal parameter identification and model reduction," *J. Guid., Control, Dyn.*, vol. 8, no. 5, pp. 620–627, Sep. 1985, doi: 10.2514/3.20031.

[34] J.-N. Juang, *Applied System Identification*. London, U.K.: Pearson, 1994.

[35] Y. Ren, C. Adams, and T. Melz, "Uncertainty analysis and experimental validation of identifying the governing equation of an oscillator using sparse regression," *Appl. Sci.*, vol. 12, no. 2, p. 747, Jan. 2022, doi: 10.3390/app12020747.

[36] D. Bertsimas and W. Gurnee, "Learning sparse nonlinear dynamics via mixed-integer optimization," *Nonlinear Dyn.*, vol. 111, no. 7, pp. 6585–6604, Apr. 2023, doi: 10.1007/s11071-022-08178-9.

[37] L. Sun, W. Li, Y. Wu, and Q. Lan, "Active vibration control of a conical shell using piezoelectric ceramics," *J. Low Freq. Noise, Vib. Act. Control*, vol. 36, no. 4, pp. 366–375, Dec. 2017, doi: 10.1177/1461348417744304.

[38] G. Song and H. Gu, "Active vibration suppression of a smart flexible beam using a sliding mode based controller," *J. Vib. Control*, vol. 13, no. 8, pp. 1095–1107, Aug. 2007, doi: 10.1177/1077546307078752.

[39] J. Yang and G. Chen, "Robust nominal model-based sliding mode robust control for vibration of flexible rectangular plate," *Appl. Math. Inf. Sci.*, vol. 7, no. 2L, pp. 671–678, Jun. 2013, doi: 10.12785/amis/072l42.

[40] K. Li, J. Ding, X. Sun, and X. Tian, "Overview of sliding mode control technology for permanent magnet synchronous motor system," *IEEE Access*, vol. 12, pp. 71685–71704, 2024, doi: 10.1109/ACCESS.2024.3402983.

[41] H. Dong, X. Yang, H. Gao, and X. Yu, "Practical terminal sliding-mode control and its applications in servo systems," *IEEE Trans. Ind. Electron.*, vol. 70, no. 1, pp. 752–761, Jan. 2023, doi: 10.1109/TIE.2022.3152018.

[42] X. Yu, Y. Feng, and Z. Man, "Terminal sliding mode control—An overview," *IEEE Open J. Ind. Electron. Soc.*, vol. 2, pp. 36–52, 2021, doi: 10.1109/OJIES.2020.3040412.

[43] S. T. Venkataraman and S. Gulati, "Control of nonlinear systems using terminal sliding modes," in *Proc. Amer. Control Conf.*, Chicago, IL, USA, Jun. 1992, pp. 891–893.

[44] M. Zhihong, A. P. Paplinski, and H. R. Wu, "A robust MIMO terminal sliding mode control scheme for rigid robotic manipulators," *IEEE Trans. Autom. Control*, vol. 39, no. 12, pp. 2464–2469, Dec. 1994, doi: 10.1109/9.362847.
[45] A. V. Oppenheim and R. W. Schafer, *Discrete-Time Signal Processing*. London, U.K.: Pearson, 2010.
[46] P. Avitabile, *Modal Testing: A Practitioner's Guide*. Hoboken, NJ, USA: Wiley, 2018, doi: 10.1002/9781119222989.
[47] S. J. Chapman. (1991). *Electric Machinery Fundamentals*. [Online]. Available: https://api.semanticscholar.org/CorpusID:106620724
[48] R. Tibshirani, "Regression shrinkage and selection via the lasso," *J. Roy. Stat. Soc. B, Stat. Methodol.*, vol. 58, no. 1, pp. 267–288, Jan. 1996. [Online]. Available: http://www.jstor.org/stable/2346178

SINA PIRAMOON (Member, IEEE) received the Ph.D. degree in mechanical engineering from Santa Clara University, in 2024. He is currently the Engineering Manager of the Laboratory Products Division, Thermo Fisher Scientific. He holds 58 U.S. and international patents in rotor design, system balancing, and consumer products. His research interests include rotordynamics, vibration control, nonlinear system identification, and data-driven applied dynamics. He is a member of American Society of Mechanical Engineers (ASME).

MOHAMMAD A. AYOUBI (Senior Member, IEEE) received the Ph.D. degree from the School of Aeronautics and Astronautics, Purdue University, West Lafayette, IN, USA. He is currently an Associate Professor with the Department of Mechanical Engineering, Santa Clara University. His general areas of expertise are multibody dynamics, rotordynamics, spaceflight dynamics, intelligent control systems, and guidance, navigation, and control (GN&C) of aerospace vehicles. He is a fellow of American Society of Mechanical Engineers (ASME), a Senior Member of American Institute of Aeronautics and Astronautics (AIAA) and American Astronautical Society (AAS), and a member of the AIAA Intelligent Systems and IEEE Aerospace Controls Technical Committees. He is also an Associate Editor of the *AIAA Journal of Spacecraft and Rockets* and IEEE TRANSACTIONS ON AEROSPACE AND ELECTRONIC SYSTEMS.

SAEID BASHASH received the Ph.D. degree in mechanical engineering from Clemson University, in 2008. He completed his two postdoctoral research appointments with the University of Michigan (2009–2010) and The Pennsylvania State University (2011–2012). He was a Senior Servo Engineer with Western Digital, from 2013 to 2015, and then joined the Department of Mechanical Engineering, San José State University, where he is currently an Associate Professor. His research interests include the modeling, system identification, and control of dynamic systems with applications in mechatronics and energy systems. He is the author or co-author of over 70 journals and conference publications in this field.